

THE STATE-OF-THE-ART *HST* ASTRO-PHOTOMETRIC ANALYSIS OF THE CORE OF  $\omega$  CENTAURI. III. THE MAIN SEQUENCE'S MULTIPLE POPULATIONS GALORE\*A. BELLINI<sup>1</sup>, A. P. MILONE<sup>2</sup>, J. ANDERSON<sup>1</sup>, A. F. MARINO<sup>2</sup>, G. PIOTTO<sup>3,4</sup>, R. P. VAN DER MAREL<sup>1</sup>, L. R. BEDIN<sup>3</sup>, AND I. R. KING<sup>5</sup>  
(Received May 22, 2017; Revised June 20, 2017; Accepted June 21, 2017)

## Abstract

We take advantage of the exquisite quality of the *Hubble Space Telescope* 26-filter astro-photometric catalog of the core of  $\omega$  Cen presented in the first paper of this series and the empirical differential-reddening correction presented in the second paper in order to distill the main sequence into its constituent populations. To this end, we restrict ourselves to the five most useful filters: the magic “trio” of F275W, F336W, and F438W, along with F606W and F814W. We develop a strategy for identifying color systems where different populations stand out most distinctly, then we isolate those populations and examine them in other filters where their sub-populations also come to light. In this way, we have identified at least 15 sub-populations, each of which has a distinctive fiducial curve through our 5-dimensional photometric space. We confirm the MSa to be split into two subcomponents, and find that both the bMS and the rMS are split into three subcomponents. Moreover, we have discovered two additional MS groups: the MSd (which has three subcomponents) shares similar properties with the bMS, and the MSe (which has four subcomponents), has properties more similar to those of the rMS. We examine the fiducial curves together and use synthetic spectra to infer relative heavy-element, light-element, and Helium abundances for the populations. Our findings show that the stellar populations and star formation history of  $\omega$  Cen are even more complex than inferred previously. Finally, we provide as a supplement to the original catalog a list that identifies for each star which population it most likely is associated with.

**Keywords:** globular clusters: individual (NGC 5139) — Hertzsprung-Russell and C-M diagrams — stars: Population II — techniques: photometric

## 1. INTRODUCTION

Omega Centauri ( $\omega$  Cen) was long believed to be a “missing link” transition object between globular clusters (GCs) and dwarf spheroidals (see, e.g., Bekki & Freeman 2003). Indeed, in August of 2001 a conference was convened in Cambridge, England, with the expressed goal of debating which bin to place it in (van Leeuwen et al. 2002).

It had been known since the seventies (Cannon & Stobie 1973) that  $\omega$  Cen’s stellar chemistry is complex, with large variations in C, N, and iron. Therefore, the discovery of multiple red giant branches (RGBs, Lee et al. 1999; Hilker & Richtler 2000; Pancino et al. 2000) that could be associated with different broad metallicity peaks was understandable and easily accepted by the astronomical community.

At the conference however, Anderson presented new results from his thesis (Anderson 1997, 2002) based on photometric techniques optimized for *Hubble Space Telescope* (*HST*) data that showed that the cluster’s main sequence (MS) was split into two clearly distinct sequences. There were several reasons that this was a surprising finding. First, spectroscopic data suggested broad overlapping distributions, not distinct, well-separated populations. Even more curious was the fact that in the *HST*  $m_{F606W}$  vs.  $m_{F606W} - m_{F814W}$  CMD explored, the reddest MS was the most populous one (see Bedin et al. 2004), while we knew from spectroscopy that the lower-

metallicity stars were the more abundant in the cluster (Norris & Da Costa 1995).

At that time, there was no plausible explanation but to assume a large difference in helium between the two MSs, as suggested since the beginning by J. Norris, the referee of the Bedin et al. (2004) paper. Indeed, even now a large He difference ( $\Delta Y \sim 0.14$ , King et al. 2012) between the two main components of  $\omega$  Cen is the only available interpretation of the photometric and spectroscopic observational facts.

The conference ended without a clear binary resolution of  $\omega$  Cen’s dwarf spheroidal or GC nature, which left it as a unique anomaly. In the years since, we have come to understand that the non-singular nature of  $\omega$  Cen’s populations are actually just an extreme example of a multiple-population phenomenon that is present in all clusters.

*HST* has played a crucial role in this research field. Piotto et al. (2015) showed that the multiple populations are present in all the 57 GCs observed within their *HST* Treasury program and related *HST* ancillary projects, though multiple populations exhibit different properties in different clusters (Milone et al. 2017a). In some cases, the population complexity is quite intriguing, as in M2 (NGC 7089, Milone et al. 2015a) or NGC 2808 (Piotto et al. 2007; Milone et al. 2015b; Bellini et al. 2015). However, none of these clusters reaches the incredible multiplicity of  $\omega$  Cen. Indeed, this paper will show that  $\omega$  Cen is even more complicated than we thought.

The results presented here are the product of a massive effort, and represent a continuation of what we published in Bellini et al. (2010). Paper I of this series (Bellini et al. 2017a) describes the photometric techniques we adopted and applied to 650 individual exposures in 26 different bands. The photometry has been corrected for differential reddening and zero-point spatial variations in Bellini et al. (2017b, Paper II). In this paper, we analyze the CMDs and the so-called “chromosome” maps (Milone et al. 2017a) of the MS of the cluster, and finally identified at least 15 distinct stellar populations. It stands to reason that a detailed understanding of the complex multiple populations in the cluster, which we will (qualita-

bellini@stsci.edu

<sup>1</sup> Space Telescope Science Institute, 3700 San Martin Dr., Baltimore, MD 21218, USA<sup>2</sup> Research School of Astronomy & Astrophysics, Australian National University, Mt Stromlo Observatory, via Cotter Rd, Weston, ACT 2611, Australia<sup>3</sup> Istituto Nazionale di Astrofisica, Osservatorio Astronomico di Padova, v.co dell’Osservatorio 5, Padova, I-35122, Italy<sup>4</sup> Dipartimento di Fisica e Astronomia “Galileo Galilei”, Università di Padova, Vicolo dell’Osservatorio 3, Padova I-35122, Italy<sup>5</sup> Department of Astronomy, University of Washington, Box 351580, Seattle, 98195, WA, USA\* Based on archival observations with the NASA/ESA *Hubble Space Telescope*, obtained at the Space Telescope Science Institute, which is operated by AURA, Inc., under NASA contract NAS 5-26555.

tively) relate to differences in Y, C, N, O, and Fe in the final part of the paper, will require a huge interpretative effort in the years to come.

The paper is organized as follows. In Section 2 we present the stellar sample. In Section 3 we describe the iterative procedures used to extract the different stellar populations. Section 4 presents an overview of the multiple stellar populations we identified, and Section 5 is dedicated to a first qualitative analysis of the color difference among the 15 populations, and to the implications in terms of differences in Y, C, N, O, and Fe content.

## 2. SAMPLE SELECTION

### 2.1. Choosing the optimal filter set

The 26 filters of our photometric catalog allow us to construct a very large number of distinct CMDs. Some CMDs based on specific filters are able to separate distinct sequences more clearly than others. Key molecular absorption bands (OH, NH, CN, CH) fall in the F275W, F336W and F438W bandpasses, making observations through these filters particularly sensitive to the fingerprints of light-element abundance differences (see, e.g., Piotto et al. 2015, their Fig. 1). The F606W and F814W bandpasses are virtually insensitive to light-element abundance variations, but are good proxies of temperature differences (and hence, He and Fe content) among MS stars of a given brightness. Photometry in most of the medium- and narrow-band filters in our catalog is available only for a subset of stars, because of the smaller field-of-view covered by these observations, the low signal-to-noise at the MS level, and the smaller number of available images (see, e.g. Fig. 1 and Table 1 of Paper I). In addition, due to crowding, photometry in WFC3/IR filters is not precise enough at the level of the MS for high-precision sequence analysis (see discussion in Sect. 3.5 of Paper I).

For these reasons, we limited our multiple-population selection procedures here to only five filters: the so-called “magic trio” (F275W, F336W and F438W), and the two optical bands F606W and F814W. Exposures taken with these five filters cover the largest FoV in our dataset, and have the largest number of contributing exposures: this guarantees us to maximize the number of MS stars that can be studied with the smallest photometric errors. Finally, a limited set of filters also helps us to minimize the impact of selection effects. We will, however, make use of a broader selection of WFC3/UVIS filters later in Sect. 5, which is dedicated to a qualitative abundance analysis of each population based on comparisons with synthetic spectra.

### 2.2. Choosing the best-measured stars

As described in Paper I, photometry in our catalog is measured through three different methods. Method one involves fitting a position and flux for each star in each exposure; it works best for bright, unsaturated stars. Method two involves forced photometry using the inner  $3 \times 3$  pixels of each source at the average position transformed into each exposure; it is best suited for relatively faint stars, while method three uses the brightest 4 pixels and weights them by the expected values of the PSF in those pixels; it is optimized for extremely low S/N stars. (We refer the interested reader to Paper I for a detailed description of the data-reduction processes.) Saturation in the five selected filters kicks in just above the base of the RGB. Here we are focused on the bright part of the MS, where method-two offers the most-precise mea-

surements. Therefore, method-two photometry is the one we make use of throughout this paper.

Our photometric catalog, containing over 470,000 sources within the central  $4'3 \times 4'3$ , offers several quality parameters that can be used to sift out poorly-measured stars, namely: (i) the quality-of-fit (QFIT), which discriminates between sources that are fit well by the PSF and extended sources or blends; (ii) the photometric rms among multiple independent measurements, (iii) the local sky-background rms, and (iv) the neighbor-contamination parameter  $o$ , which tells us the fraction of the flux due to neighbors within the PSF fitting radius of of a given star and the star’s flux itself.

To select the best-measured stars, we started from the star list we used in Paper II to derive a high-precision, differential-reddening map of the core of the cluster (see their Sect. 2.2 for details). In a nutshell, this star list is obtained by removing poorly-measured sources according to all four of the quality parameters mentioned above. In addition, the list contains only stars with a measured proper motion consistent with the cluster’s bulk motion. The list used in Paper II contains 72,609 well measured, proper-motion-selected cluster stars.

We showed in Paper II that differential-reddening in the core of the cluster can vary by up to  $\sim 10\%$ , with a typical standard deviation of about 4%. This is generally not a concern for most scientific applications, since the most-relevant features on a CMD can be easily recognized without the need for a differential-reddening correction. Here we aim at characterizing the finest details in a CMD, and we must correct our photometry for differential-reddening effects. To do this, we closely followed the prescriptions given in Paper II. To minimize the impact of possible systematic errors related to edge effects in the differential-reddening correction, we further restricted our star list to include only those stars that had enough reddening-reference stars within 600 pixels (or  $24''$ ) to enable an empirical differential-reddening correction. This can easily be done using the information contained in the “radius map” extension of the `fits` file we published in Paper II. This restriction limited the area covered by selected stars from about  $4'3 \times 4'3$  to the inner  $3'3 \times 3'3$ .

The final catalog contains 69 536 high-photometric-quality stars measured in all five filters, and extends from about 2 magnitudes above the turn-off ( $m_{F606W} \sim 16$ ) down to about 3.5 magnitudes below the turn-off ( $m_{F606W} \sim 21.5$ ). The limiting factor at the faint end is represented by the insufficient signal-to-noise in F275W, while saturation dictates the bright-end limit.

## 3. THE MAIN SEQUENCE UNFOLDS

The MSs of the different stellar populations in  $\omega$  Cen typically overlap each other at different magnitude levels in different CMDs, and teasing them apart involves a careful, iterative process. We adopted the following general approach to identify distinct populations:

- We start with a preliminary selection of a given population on the CMD where this population stands out most clearly (as a spread sequence or a bimodal color distribution at fixed magnitude). We experimented with all possible combinations of filters to construct CMDs, and selected the one that allows the best separation between stars of the analyzed population and the rest of the MS. This initial, preliminary selection invariably contains contaminants from other populations.

## MSa SELECTION CRITERIA

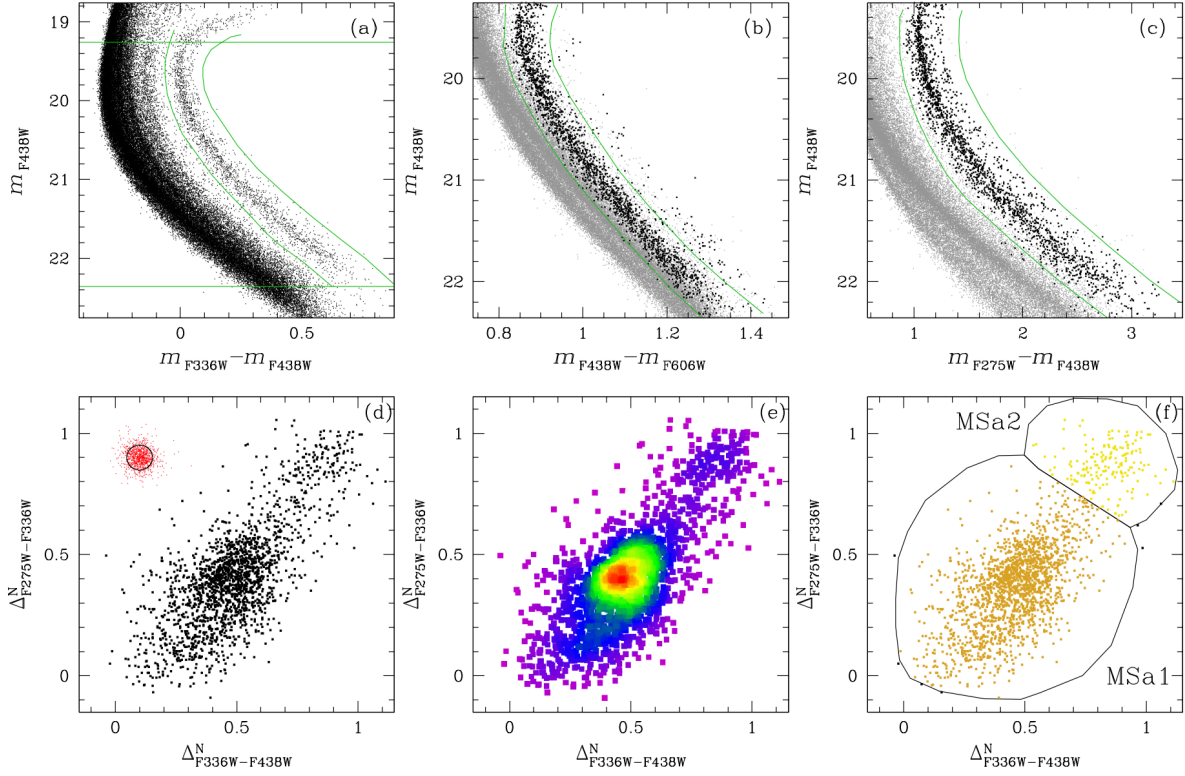


**Figure 1.** Illustration of the selection procedures we applied to isolate MSa stars. (a): Preliminary selection of MSa candidates on the  $m_{F336W} - m_{F438W}$  CMD (within the green lines). (b) and (c): selection refinements using two CMDs of different color. In black we show MSa stars selected from the previous panel, in gray the rest of the MS. Rejected stars are those outside the two green lines. In panel (d) we show the  $\Delta_{m_{F275W} - m_{F336W}}^N$  vs.  $\Delta_{m_{F336W} - m_{F438W}}^N$  chromosome map of MSa stars that survived our selections (a)+(b)+(c), in black. Red points show the distribution of a single sequence as predicted by only photometric and differential-reddening-correction errors. The Hess diagram of the chromosome map is in panel (e). It is clear that there is a main component around (0.45,0.45) in the Hess diagram, which elongated shape toward (0,0) might indicate additional substructures, and a secondary component at around (0.9,0.9). We defined two MSa subpopulations in Panel (f), corresponding to the two main clumps in the chromosome map: MSa1 (in dark yellow) and MSa2 (in light yellow).

- We plot these preliminary-selected stars on a few different CMDs in which outliers are most-easily identified and rejected. These CMDs are again chosen by trial-and-error as those optimizing the identification of outliers.
- We make use of rectified and parallelized two-color diagrams, so-called “chromosome maps”, to highlight finer population structures (see Milone et al. 2015a,b).
- Once stars belonging to a given population have been identified and selected, we removed them from the list, and repeated the process on a different population.
- We repeat the entire process until no more clear distinct sequences can be identified.

This iterative procedure of population tagging, refining, selecting and removing (TRSR) will prove to be quite effective. Given the tangled weave intertwined by the MPs on the MS of  $\omega$  Cen, we began by identifying those populations that clearly stand out on either side of the MS. Then, we proceeded toward the more intricate central MS region.

For consistency and simplicity, in the following we will always use  $m_{F438W}$  magnitudes as the y axis of our CMDs, while we let the CMD color vary. Hence, we will hereafter identify a CMD solely by its color (unless specifically stated otherwise).

### 3.1. The MSa

The MSa is clearly isolated from the rest of the MS in the  $m_{F336W} - m_{F438W}$  CMD (panel a of Fig. 1). We limited our selection in the magnitude range  $19.26 \leq m_{F438W} \leq 22.36$ . The bright limit is slightly above the MSa turn-off, while beyond the faint limit the number of available MSa stars suddenly drops, due to incompleteness. (Because of the peculiar isolation of MSa stars from the rest of the MS, we pushed the bright limit above the turn-off level. The bright limit will be set to a fainter level,  $m_{F438W} = 20.16$ , for the analysis of the other populations.) Magnitude cuts are indicated by the two horizontal green lines in panel (a). We drew by hand the two lines (also in green, following the MSa profile) that delimit the blue and the red boundaries of MSa stars.

We decided to manually define the color boundaries used to delimit the MSa (as well as all those of all other MSs) be-

cause, although an automatic procedure would be in principle more easily repeatable, no machine can be as accurate and precise as the human eye for this task. Our selections are always clearly highlighted at each stage in all the figures.

Next, preliminary-selected MSa stars are plotted on the  $m_{F438W} - m_{F606W}$  CMD (in black in panel b). The remaining, unidentified MS stars are shown in gray. A few outliers (possibly binaries and/or stars that do not belong to the MSa population) clearly stand out, mostly on the red side of the CMD. We restricted our MSa selection to only those stars within the two green lines in panel (b). (For consistency, unless stated otherwise, green lines will hereafter always indicate our selection boundaries, black points will mark selected stars from the previous panel, while all other stars will be in gray.) Panel (c) of Fig. 1 shows the  $m_{F275W} - m_{F438W}$  CMD of the surviving MSa stars that passed both selections of panels (a) and (b). We removed a few additional outliers from our MSa candidates (black points outside the two green lines). Note that on this panel we can clearly distinguish a secondary, less-populated sequence of stars to the red side of the main distribution. As we have shown in Bellini et al. (2010, their Fig. 13 and related discussion), these stars are not binaries and constitute a distinct subpopulation of the MSa. In fact, for  $m_{F438W} < 20$ , the MSa sequence is almost vertical, and any binary sequence made up of MSa stars is going to necessarily merge with the MSa stars themselves on a CMD. What we see in panel (c) (as well as in panel a), instead, is that the secondary population runs parallel to MSa stars also for  $m_{F438W} < 20$ .

“Chromosome” maps are a very powerful tool that have been used extensively over the last few years to reveal multiple-population substructures in GCs (see, e.g., Milone et al. 2015a,b, 2017a, and references therein). Briefly, the construction of a chromosome map begins by tracing two guide lines enclosing a given population in a CMD based on a particular color (e.g.,  $m_{F336W} - m_{F438W}$ ). These two lines are then used to rectify and parallelize the population sequence<sup>1</sup>, which then appears as a vertical distribution of stars of constant width in the  $\Delta_{F336W-F438W}^N$  pseudo CMD (where  $\Delta_{F336W-F438W}^N$  indicates the rectified and parallelized pseudo color). In the pseudo CMD, the bluer and redder guide lines used in the rectification and parallelization process (in other words, a homographic transformation of the CMD plane) are transformed into vertical lines at abscissa 0 and 1, respectively (see Milone et al. 2015a,b for more details). The same procedure can be applied to a CMD based on a different color, e.g.  $m_{F275W} - m_{F336W}$  to obtain the pseudo-color  $\Delta_{F275W-F336W}^N$ . The two pseudo colors derived this way are then plotted one against the other to create a chromosome map. (Note that chromosome maps can also be constructed using color indexes instead of colors. A color index is defined as a difference between two colors with a filter in common, e.g.:  $C_{F275W,F336W,F438W} = (m_{F275W} - m_{F336W}) - (m_{F336W} - m_{F438W})$ , where the filter in common in this case is F336W, see also Milone et al. (2013); Piotto et al. (2015) and references therein.)

The  $\Delta_{F275W-F336W}^N$  vs.  $\Delta_{F336W-F438W}^N$  chromosome map of selected MSa stars is shown in panel (d) of Fig. 1 (black points). In both the  $m_{F275W} - m_{F336W}$  and  $m_{F336W} - m_{F438W}$  CMDs we simulated a single sequence of stars, the color

spread of which is defined by photometric and differential-reddening-correction errors only, and passing in between the two lines that were used to rectify and parallelize the population sequence in each CMD. We computed the  $\Delta_{F275W-F336W}^N$  vs.  $\Delta_{F336W-F438W}^N$  values for this simulated sequence to show how the chromosome map of a single sequence would appear (red points in panel d). The black ellipse encloses the 68.27 percentile of the simulated stars. It is clear that the chromosome map of selected MSa stars is much wider (and clumpy) than what photometric and differential-reddening-correction errors would predict.

The Hess diagram of the chromosome map of selected MSa stars is shown in panel (e). The color mapping of this and the following Hess diagrams goes from purple (lowest density) to blue, green (average density), yellow and red (highest density). The Hess diagram is provided with the only purpose of giving the reader a qualitative and clearer sense of the distribution of stars in the chromosome map. In panels (d) and (e) we can clearly distinguish two clumps: a main clump at about (0.45, 0.45), with a tail extending down to (0.1, 0.0), and a second, less-populated clump located at about (0.9, 0.9). The tail of the main clump could be a hint of a spread in light-element abundances of the main-clump subpopulation, or it could even represent a distinct subpopulation of stars partially overlapping the main clump in the chromosome map. On the other hand, the tail could also be the result of a non-optimal subtraction of outliers. Given the uncertain nature of the tail, in panel (f) we conservatively defined only two subpopulations of MSa: the MSa1 (dark yellow) and the MSa2 (light yellow), within the black envelopes. Stars outside these black envelopes are rejected. The selections defined in panel (f) set the final sample of the MSa subpopulations. This analysis confirms the findings of Bellini et al. (2010) that the MSa population is split into two components. The inclusion of the tail into the MSa1 selection will have little or no effect on the average properties of the MSa1 subpopulation, given the relatively small number of stars in the tail with respect to the total number of MSa1 stars.

### 3.2. The bMS

The second easiest population to isolate is the bMS, which typically stands out quite clearly on the blue side of the MS in most CMDs of  $\omega$  Cen, in particular in the  $m_{F438W} - m_{F814W}$  CMD shown in panel (a) of Fig. 2. On this and the following panels of the figure, all previously-identified stars (in this case, MSa1 and MSa2 stars) have been removed, in order to facilitate the selection of the remaining populations. For clarity, in panel (a) we plotted a randomly-selected 30% of the stars.

To select bMS stars, we kept the same faint limit as for the MSa, i.e.  $m_{F438W} = 22.36$ , but we had to lower the bright limit to  $m_{F438W} = 20.16$ . In fact, at magnitudes brighter than  $m_{F438W} = 20.16$ , the bMS and the rMS become too close to each other (and eventually overlap below the turn off) in every CMD regardless of the adopted color baseline. As we did for the MSa, we drew by hand two lines (also in green) defining the color boundaries of our preliminary-selected bMS stars. At this stage, both boundaries are purposely generous and necessarily enclose rMS contaminants. We want to be as inclusive as possible in our first selection, so to start from a sample containing most –if not all– bMS stars. Contaminants will be rejected later using CMDs based on different colors, as we have done for MSa stars.

<sup>1</sup> Basically, to the color of each star we subtract the color of the blue-boundary line at the same magnitude level of the star, and then we divide this quantity by the difference in color between the red- and the blue-boundary lines (again at the same magnitude level).



## bMS SELECTION CRITERIA

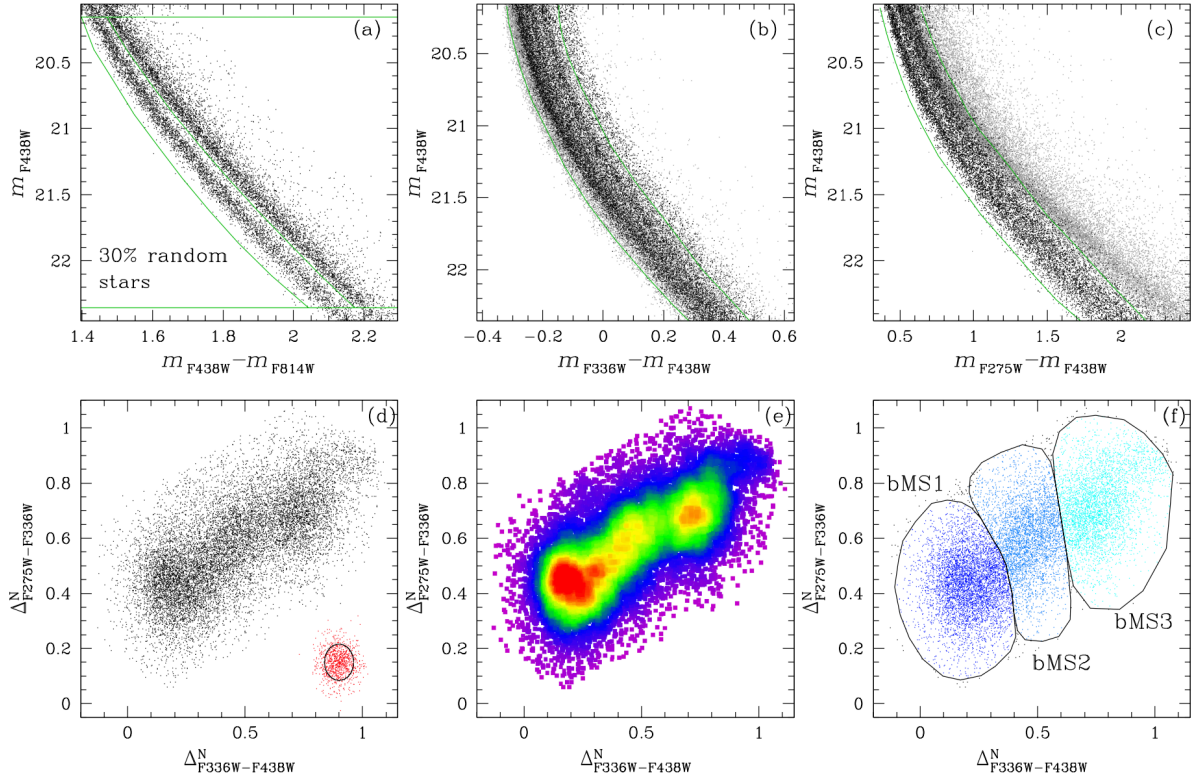


**Figure 2.** These six panels are arranged in a similar way as those of Fig. 1, but this time we show how we selected bMS stars. We preliminary selected bMS stars on the  $m_{F438W} - m_{F814W}$  CMD in panel (a), within the green lines. This particular CMD offers the clearest separation between bMS and rMS stars. For clarity, we plotted a randomly-selected 30% of the stars. Already identified MSa1 and MSa2 stars have been removed from the CMD. Preliminary-selected bMS stars are further refined using the  $m_{F336W} - m_{F438W}$  and  $m_{F275W} - m_{F438W}$  shown in panels (b) and (c). As we did for Fig. 1, survived stars from the previous panel are in black, while rejected stars are in gray.  $\Delta_{m_{F275W} - m_{F336W}}^N$  vs.  $\Delta_{m_{F336W} - m_{F438W}}^N$  chromosome map and Hess diagram are in panels (d) and (e), respectively. Panel (e) reveals at least three main subcomponents of the bMS, that we identify as bMS1 (dark blue), bMS2 (azure), and bMS3 (light blue) in panel (f).

In panel (b) of Fig. 2 we show the  $m_{F336W} - m_{F438W}$  CMD of preliminary-selected bMS stars from panel (a). Stars rejected in panel (a) are in gray. The bMS on this CMD is significantly spread in color (with hints of substructures). A small fraction of stars are smeared toward redder colors. We removed this red tail of stars, together with a few other outliers on the blue side, using the two green lines. A further selection refinement is applied on the  $m_{F275W} - m_{F438W}$  CMD (panel c). Note that the bulk distribution of bMS stars is also spread in panel (c), with hints of a split.

The  $\Delta_{m_{F275W} - m_{F336W}}^N$  vs.  $\Delta_{m_{F336W} - m_{F438W}}^N$  chromosome map of survived bMS stars after the selections we applied in panels (a)+(b)+(c) is shown in black in panel (d). In red the expected distribution of a single sequence of stars, based on only photometric and differential-reddening-correction errors. The ellipse encloses the 68.27 percentile of the single-sequence distribution. The Hess diagram of the chromosome map is presented in panel (e). Three main clumps of stars can be clearly seen in these two panels. All of them exhibit some degree of substructures. In particular, the bluer clump, located at (0.2, 0.4), shows a red tail that pushes out towards the central clump, while another tail of points emerges from the redder

clump, located at (0.75, 0.7) and runs out to about (1.1, 0.9).

Following the same conservative approach we applied to MSa stars, we defined three subpopulations of the bMS in panel (f): the bMS1 (blue), the bMS2 (azure), and the bMS3 (cyan), each defined as all stars within the respective black envelope.

The identification of the bMS2 might appear less obvious than that of the other two bMS subpopulations, and one could argue that the bMS2 is simply part of the tail of the distribution of bMS1 stars. It should be noted, however, that the over-density at the center of the bMS2 distribution is about 3 sigmas away from the peaks of both the bMS1 and the bMS3, in terms of photometric and differential-reddening errors alone. Moreover, if errors alone are the cause of the central over-density that we identify as the bMS2 — which is redder than the bMS1 in the  $m_{F336W} - m_{F438W}$  CMD —, then stars of the “bMS2” would have an equal chance of being bluer or redder than the bMS1 in another CMD based on different filters. We see, instead, that bMS2 stars are systematically bluer than bMS1 stars in the  $m_{F275W} - m_{F336W}$ : a particular characteristic that implies a different light-element abundance for the bMS1 and the bMS2. Finally, it could be that the bMS1 pop-

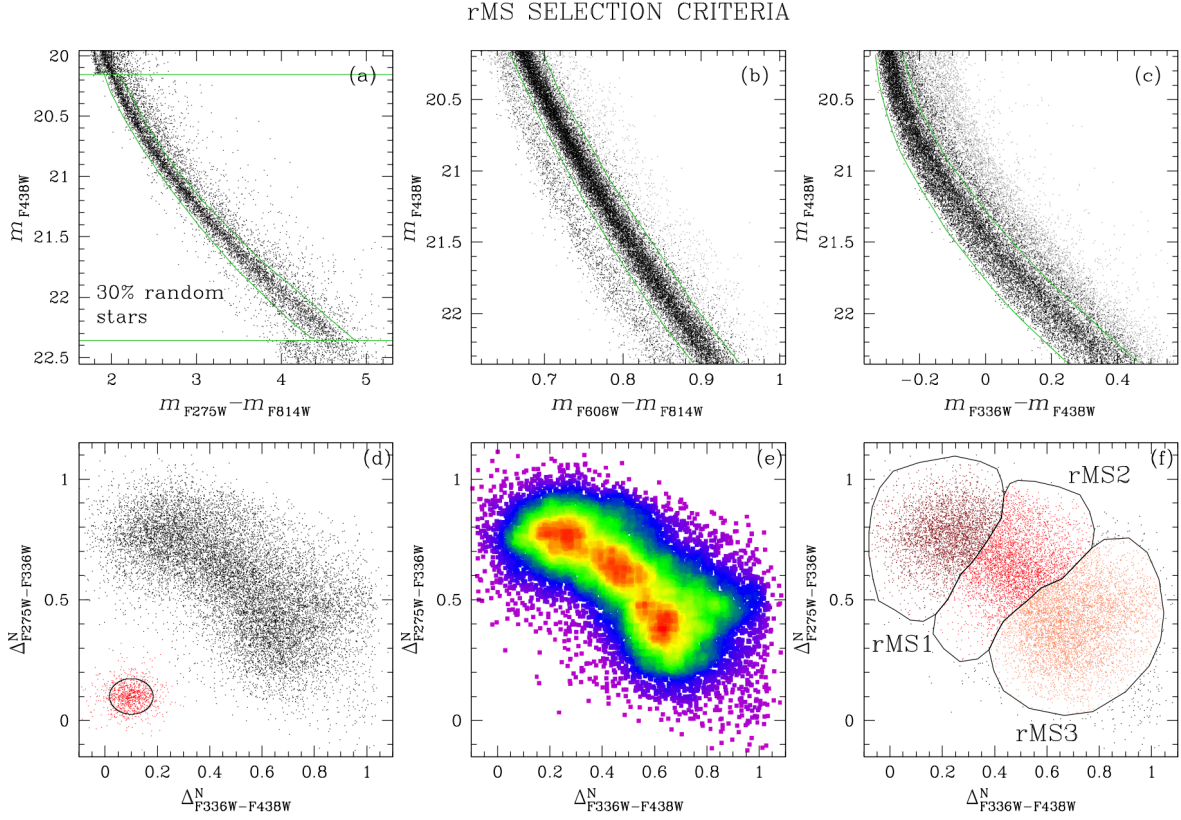


**Figure 3.** Similar to Fig. 1, but for the rMS. As for the bMS, the Hess diagram in panel (e) reveals at least three main subcomponents, labeled as rMS1 (brown), rMS2 (red), and rMS3 (orange) in panel (f).

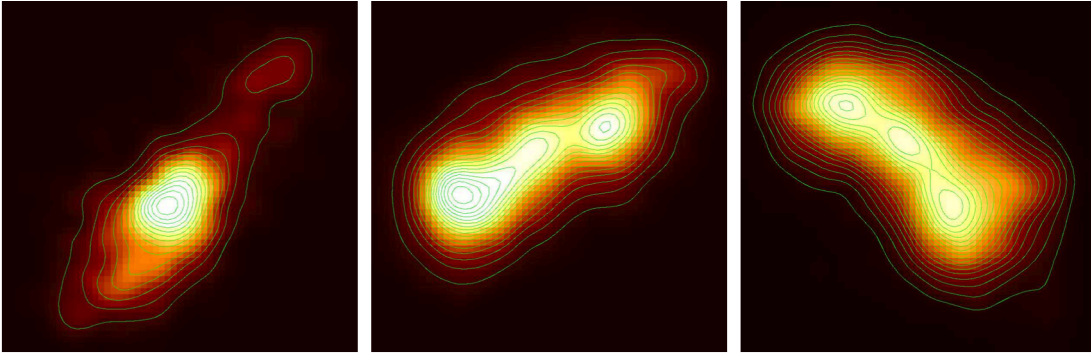


**Figure 4.** Gaussian-smoothed  $\Delta_{m_{F275W}-m_{F336W}}^N$  vs.  $\Delta_{m_{F336W}-m_{F438W}}^N$  chromosome maps for the MSa (left), the bMS (middle), and the rMS (right) subpopulations. Isodensity contours are shown in green. Axes quantities, scales and ranges are the same as the corresponding panels (d), (e) and (f) of each population selection.

ulation formed over a relatively long period of time, and its stars contain a spread—as opposed to a split in the case of two short star-formation bursts—in light-element abundance: spread that we have identified as the bMS2.

All of these caveats notwithstanding, for the time being let us consider the bMS1 and the bMS2 as two distinct subpopulations.

It stands to reason that bMS1 and bMS3 stars will neces-

sarily be contaminated by some bMS2 stars, and vice versa. Nevertheless, the average properties of stars within each subpopulation selection will still be representative of the subpopulation itself.

### 3.3. The rMS

Once bMS and MSa stars have been removed, rMS stars stand out quite clearly in the CMD, e.g. in the  $m_{F275W} -$

$m_{F814W}$  CMD we show in panel (a) of Fig. 3. For clarity, in this panel we plotted a randomly-selected 30% of the stars, as we did in panel (a) of Fig. 2. We kept the same magnitude limits as for the bMS (green horizontal lines), and preliminary selected (by hand) rMS stars on this panel by means of the two diagonal green curves.

Selected stars are then plotted in black in the  $m_{F606W} - m_{F814W}$  CMD of panel (b). What appeared as a single sequence in panel (a) is now clearly split into two sequences: a well defined, more-populated sequence on the red side and a less-populated sequence on the blue side of the bulk population. The  $m_{F606W} - m_{F814W}$  CMD, which is mostly unaffected by light-element-abundance variations, helps us in distinguishing populations with different He enhancement. The sequence of stars on the blue side of the bulk population is therefore likely to be He-enhanced with respect to the bulk population itself.<sup>2</sup> Since the rMS should be made up of first-generation, Fe-poor and He-normal stars (Piotto et al. 2005) we removed stars on this bluer sequence from our rMS selection, together with a few outliers on the red side of the bulk population. We will return to this blue sequence in the next subsection. An additional rejection of likely outliers is performed on the  $m_{F336W} - m_{F438W}$  CMD of panel (c).

Panel (d) shows the  $\Delta_{m_{F275W}-m_{F336W}}^N$  vs.  $\Delta_{m_{F336W}-m_{F438W}}^N$  chromosome map of selected rMS stars (in black) and the error distribution (in red). The corresponding Hess diagram is in panel (e). As for the bMS, three main clumps of stars stand out clearly in the chromosome map, with the rightmost clump, located at (0.6, 0.3) possibly showing a scarcely-populated tail of stars extending towards (0.9, 0.0). Again, we conservatively defined just three rMS subpopulations in panel (f): rMS1 (brown), rMS2 (red), and rMS3 (orange). As for the bMS subpopulations, any slight cross-contamination of the rMS subpopulations should not affect their general properties.

It is worth noting that—in contrast to the behavior of MSa and bMS stars in the  $\Delta_{m_{F275W}-m_{F336W}}^N$  vs.  $\Delta_{m_{F336W}-m_{F438W}}^N$  chromosome map, which both showed populations aligned from the bottom-left to the upper-right, here we see that the rMS stars are aligned from the bottom-right to the upper-left. We will return to this property in Sect. 5.

### 3.4. Hidden MS populations

In the previous subsections, we identified stars belonging to the three main populations of  $\omega$  Cen, namely: the MSa, the bMS, and the rMS. Between  $20.16 \leq m_{F438W} \leq 22.36$ —the magnitude interval we used to select both the bMS and the rMS—we have a total 39 529 high-photometric-quality MS stars. In this magnitude range, the selected MS populations (and their subpopulations) account for:

- MSa: 1394 stars ( $3.53 \pm 0.10\%$ ), of which 1283 stars ( $3.25 \pm 0.09\%$ ) belong to the MSa1 subpopulation, and 111 stars ( $0.28 \pm 0.03\%$ ) are MSa2 stars.
- bMS: 12 776 stars ( $32.32 \pm 0.33\%$ ), so divided: 5141 ( $13.01 \pm 0.19\%$ ) bMS1 stars, 3683 ( $9.32 \pm 0.16\%$ ) bMS2 stars, and 3952 ( $10.00 \pm 0.17\%$ ) bMS3 stars.
- rMS: 13 124 stars ( $33.20 \pm 0.33\%$ ), divided into 3739 ( $9.46 \pm 0.16\%$ ) rMS1 stars, 3838 ( $9.71 \pm 0.16\%$ ) rMS2 stars, and 5547 ( $14.03 \pm 0.20\%$ ) rMS3 stars.

<sup>2</sup> Note that MSa and rMS stars are overlapped in the  $m_{F606W} - m_{F814W}$  CMD, with MSa stars being mostly parallel to bMS stars. More in Sect. 4.

The quoted errors correspond to Poisson errors only. Figure 4 provides an alternative view of the chromosome maps of the three populations. Panels from left to right show a bichromatic (red to yellow, low to high) Gaussian-smoothed version of panels (e) of Figs. 1, 2 and 3, respectively. Iso-density contours are also shown, for clarity. These Gaussian-smoothed plots emphasize better some subtle features present in the chromosome maps, and should be used together with the chromosome maps and the Hess diagrams in panels (d) and (e) of Figs. 1, 2 and 3 to qualitatively assess the efficacy of our TRSR method.

Overall, selected populations account for only  $\sim 69\%$  of MS stars. There are still 12 229 unidentified stars (a number comparable in size to that of bMS or rMS stars!) that seemingly do not belong to either the MSa, the bMS, or the rMS. Our TRSR method is limited to only four passages, hence selection effects alone are unlikely to be the cause of such a large number of still unidentified stars. When we selected rMS stars in panel (b) of Fig. 3, it was clear that we rejected stars belonging to a previously-unidentified population. Possibly, something similar—but less obvious—also happened when we rejected what we thought were bMS outliers in panel (b) of Fig. 2.

So far, we have identified a total of 8 subpopulations in  $\omega$  Cen, which already make this cluster the most complex of all GCs. Nevertheless, it seems that more is left to unravel. Our TRSR method proved to work reasonably well so far. Now, what happens if we remove all 8 subpopulations from a CMD and apply the same selection procedures to what is left?

### 3.5. The MSd

Besides MSa1 and MSa2 stars, the remaining 6 subpopulations (bMS1, bMS2, bMS3, rMS1, rMS2 and rMS3) are mostly overlapped with each other in the  $m_{F336W} - m_{F814W}$  CMD. We show this CMD in panel (a) of Fig. 5. Stars belonging to previously-identified subpopulations are color-coded accordingly. The two horizontal green lines mark the magnitude interval used to select bMS and rMS stars. The vast majority of unidentified stars on this CMD lie to the red side of both bMS and rMS subpopulations, and to the blue side of MSa stars.

In order to show that these unidentified stars are unlikely to be all unresolved binaries and/or blends, we marked with a blue line the locus of equal-mass bMS1-bMS1 binaries, being bMS1 stars the bluest/faintest among the 8 identified subpopulations. Equal-mass binaries made up by any other subpopulation combination are expected to be brighter/redder than this blue line. Typically, the mass-ratio distribution of binary stars is found to be almost flat for most of globular clusters, with an overdensity near the equal-mass binary sequence (Milone et al. 2012a). This translates into a close-to-uniform distribution of binaries between a single-star sequence and the equal-mass binary sequence.

What we see in panel (a) of Fig. 5 is, instead, that still-unidentified stars lie in close proximity of the bulk of the MS, and significantly far from the blue line. Unless the vast majority of binaries in  $\omega$  Cen are made up of stars where the primary is always far more massive than the secondary—an extremely unlikely event indeed—it is apparent that the unidentified stars cannot be all binaries.

The blend hypothesis can also be quickly dismissed. Our star list contains high-quality photometric measurements in five filters, from the near UV to the  $I$  band. Let us suppose that two stars are so close to each other on the FoV that our

## MSd SELECTION CRITERIA

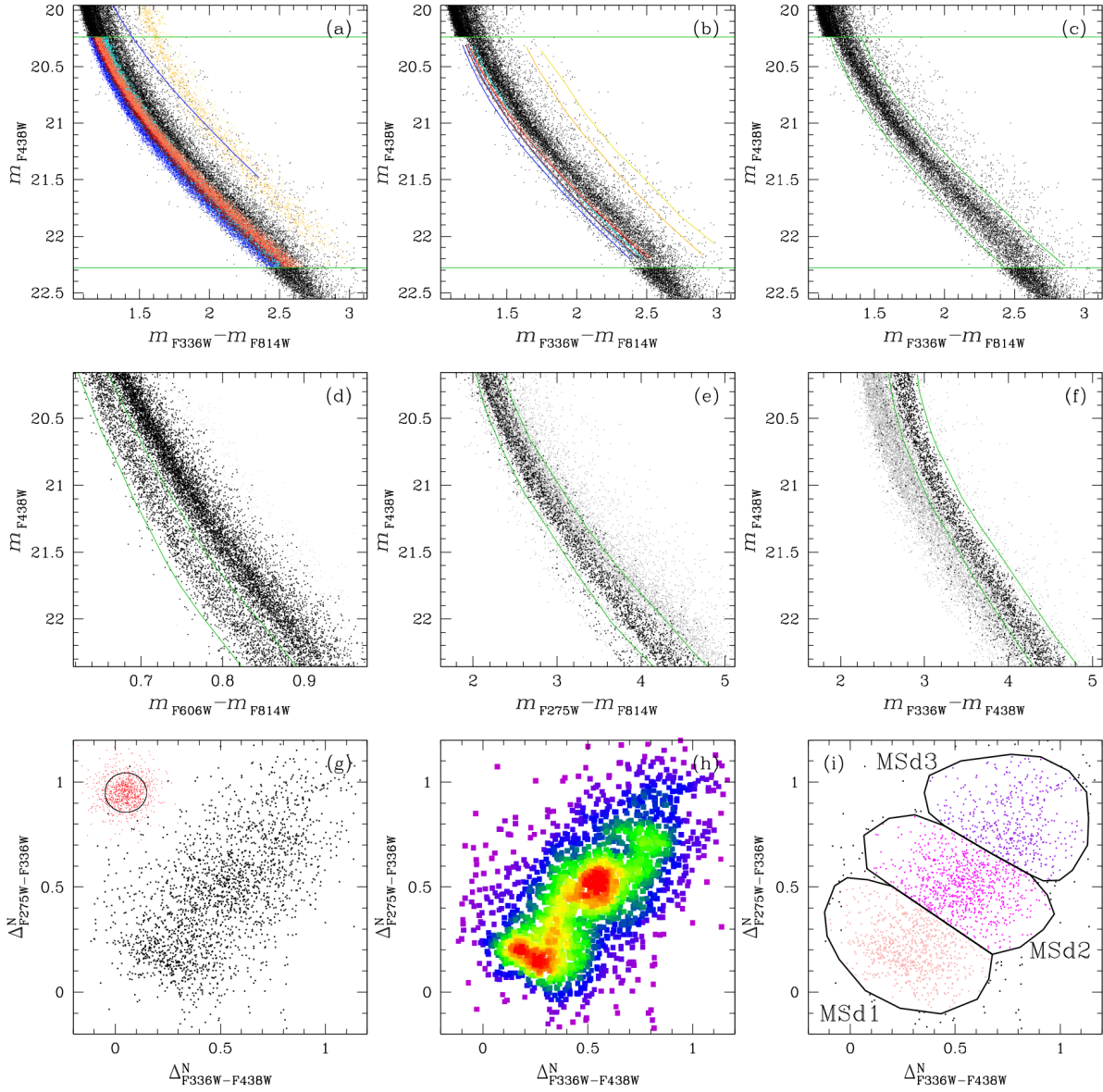


**Figure 5.** (a)  $m_{F336W} - m_{F814W}$  CMD of the MS of  $\omega$  Cen. Stars belonging to previously-identified subpopulations are color-coded accordingly. Unidentified stars are in black. Panel (b) shows the same CMD as in panel (a), in which now color-coded fiducial lines replace identified stars. Panel (c) is similar to that of panels (a) and (b), but now only unidentified stars are shown. On this panel, we preliminary selected stars that seem to form a well-defined sequence. These stars are plotted in (d) on the  $m_{F606W} - m_{F814W}$  CMD, where they clearly split into two components. On the rest of the figure we focus on the less-populated blue component, that we hereafter call as the MSd. Panels (e) and (f) illustrate our selection refinements for MSd stars. The chromosome map (g) and Hess diagram (h) of MSd stars reveal three main subpopulations, that we define in panel (i) as MSd1 (pink), and MSd2 (magenta), and MSd3 (purple).

reduction software measured only one position and magnitude for them. Then, unless these two stars have a very similar luminosity in all five filters (again, a very unlikely event), the measured position of the blend will be much closer to the hotter source in F275W, and much closer to the colder source in F814W, because of the negligible contribution of the other source in these bands. This would result in an artificially increased positional rms for the blend, and the blend would have been rejected in our PM selections. Even in the case where the

two sources have a similar luminosity in one band, then the QFIT parameter would tell us that the PSF fit was not optimal, and the blend would have been rejected in our photometric selections. Of course, we cannot exclude that a few blends survived all the astro-photometric selections we applied and made it into our final star list, but these blends are expected to be a rarity, not 30% of the MS stars.

Panel (b) of Fig. 5 is similar to panel (a), except that stars of the 8 previously-identified subpopulations have been removed



## MSe SELECTION CRITERIA

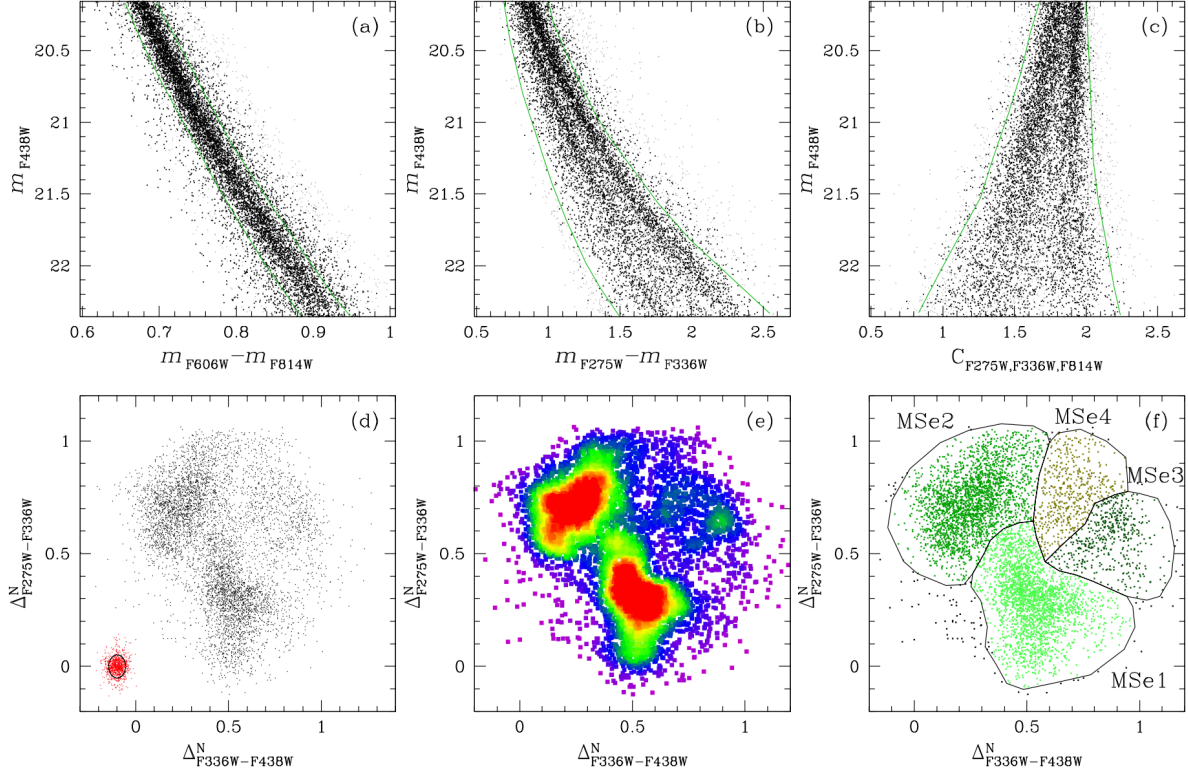


**Figure 6.** Panel (a) is a replica of panel (d) of Fig. 5, in which we also removed MSd stars. The remaining stars (hereafter MSe) form a well-defined sequence on this plane, which we select and further refine in panels (b) and (c). Note that in both panels (b) and (c) MSe stars appear to be split into two sequences. Also note that in panel (c) we use the  $C_{F275W, F336W, F814W}$  pseudo color CMD instead of a normal CMD. The chromosome map and the Hess diagram shown in panels (d) and (e), respectively, reveal a quite complex picture, with two main clumps of stars with asymmetric shape and two additional less-populated clumps that occupy a well-defined region. These four clumps are identified in panel (f) as: MSe1 (lime), MSe2 (green), MSe3 (dark green) and MSe4 (olive).

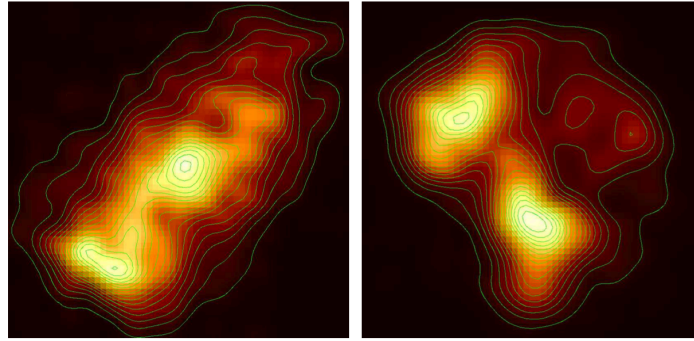


**Figure 7.** Gaussian-smoothed  $\Delta_{m_{F275W} - m_{F336W}}^N$  vs.  $\Delta_{m_{F336W} - m_{F438W}}^N$  chromosome maps for the MSd (left), the MSe (right) subpopulations. Isodensity contours are shown in green. Axes quantities, scales and ranges are the same as the respective panels (d), (e) and (f) of each population selection.

and replaced by the subpopulation fiducial lines (color-coded accordingly). Fiducial lines are obtained via least-squares fitting of a third-order polynomial to the stars of each population

on a CMD. In panel (c) we show the same CMD of panels (a) and (b), but for unidentified stars only. These stars appear to form a single, well-defined sequence on the  $m_{F336W} - m_{F814W}$

CMD, which we preliminarily select by means of the two green diagonal lines (drawn by hand).

Panel (d) shows the  $m_{F606W} - m_{F814W}$  CMD of these selected stars in black. Surprisingly, what seemed to be a single sequence in panel (c) now splits into two components. A quick cross-check revealed that the blue component is made up of the same stars that we rejected during our rMS selection procedures (panel b of Fig. 3). Despite the similarities between panel (d) of Fig. 5 and panel (b) of Fig. 3, the red component in Fig. 5 is *not* made by rMS stars, as rMS stars have already been removed from the CMD. The red component we see in panel (d) of Fig. 5 and rMS stars simply happen to overlap each other in the  $m_{F606W} - m_{F814W}$ -baseline CMD.

Since the  $m_{F606W} - m_{F814W}$  color is a clear tracer of He and Fe abundance variations, the two components we see in panel (d) are very likely to have different He abundances and/or different metallicity. They exhibit a similar behavior to that of bMS and rMS stars, i.e., they are clearly split in  $m_{F606W} - m_{F814W}$ , but are overlapped in  $m_{F336W} - m_{F814W}$ .

First, we focused on the blue component, which we will hereafter call as “MSd”. MSd stars are preliminarily selected (green lines) in panel (d). We further refined the MSd sample by removing a few outliers using the  $m_{F275W} - m_{F814W}$  and  $m_{F336W} - m_{F438W}$  CMDs (panels (e) and (f), respectively).

The chromosome map and the Hess diagram of selected MSd stars are shown in panels (g) and (h), respectively. The Hess diagram highlights two main clumps of stars located at (0.25,0.15) and (0.55,0.5), and a less-populated clump at (0.8,0.7). We identified these three clumps in panel (i) as the subpopulations MSd1 (pink), MSd2 (magenta) and MSd3 (purple). Another hint about the possible chemical similarity between MSd and bMS stars is given by the similar orientation of the respective subpopulations on the chromosome map.

The identification of the MSd3 subpopulation is somewhat less obvious than that of the other two MSd subpopulations, and the same arguments that we made for the bMS2 can be applied to the MSd3 as well.

### 3.6. The MSe

Now, let us focus our attention on the red component (hereafter MSe) we left aside in panel (d) of Fig. 5. Panel (a) of Fig. 6 is similar to panel (d) of Fig. 5, but here we have removed MSd stars. In this panel we preliminarily selected MSe stars as those within the two green lines, and we further refined the MSe sample as shown in panels (b) and (c). Note that this time panel (c) shows the pseudo-CMD based on the color index  $C_{F275W,F336W,F814W}$ , instead of a normal CMD as it was the case for the previous figures. In both panels (b) and (c), MSe stars clearly split into two predominant sequences.

Panels (d) and (e) of Fig. 6 show the chromosome map of selected MSe stars and its Hess diagram, in which the two sequences we saw in panels (b) and (c) stand out clearly as the two main clumps, located at about (0.2,0.7) and (0.5,0.3). It is worth noting that the shape of both these clumps is far from being symmetric: a possible indication of substructures. There are also two additional, less populated clumps centered at around (0.65,0.7) and (0.9,0.65). Since these two lesser clumps are located in distinct regions of the chromosome map, significantly far from the two main components, we propose that they actually constitute two additional subpopulations of the MSe (this can be better seen in Fig. 7). In panel (f) we therefore selected the following four MSe subpopulations: MSe1 (lime), MSe2 (green), MSe3 (dark green),

and MSe4 (olive).

Please note that the single-population error distribution (red points in panel d of Fig 6) is comparable in size to that of the MSe3 and the MSe4, but significantly smaller than the MSe1 and the MSe2, further suggesting that what we have defined as MSe1 and MSe2 could likely hide additional subcomponents. Moreover, both the Hess diagram of the chromosome map (panel e of Fig 6) and its Gaussian-smoothed representation (right panel of Fig. 7 do not do justice to highlight the actual significance of the MSe3 and MSe4 peaks. We employed a linear color-mapping for the Hess diagrams and a linear isodensity contour spacing for the Gaussian-smoothed maps of all the previous populations. For consistency, we also adopted the same scheme for the MSe. Since the MSe subpopulation relative fraction can vary by up to a factor of 5, a logarithmic color mapping and contour spacing might have been more appropriate. Finally, we remark that MSe3 and MSe4 stars have, on average, the same photometric errors as MSa2 stars, which are again about a factor of five less numerous than both the MSe3 and the MSe4.

In summary, we have discovered 2 major new populations on the MS of  $\omega$  Cen, which were previously hidden by bMS and rMS stars. We call these new populations MSd and MSe. The MSd is in turn made up of three subpopulations (MSd1, MSd2 and MSd3), and shares similar properties to bMS stars. The MSe is made up of four subpopulations and shares similar properties to rMS stars. The MSd and MSe populations account for:

- MSd: 2016 stars ( $5.10 \pm 0.12\%$ ), of which 757 ( $1.92 \pm 0.07\%$ ) are MSd1 stars, 819 ( $2.07 \pm 0.07\%$ ) are MSd2 stars, and 440 ( $1.11 \pm 0.05\%$ ) are MSd3 stars.
- MSe: 6129 stars ( $15.51 \pm 0.21\%$ ), subdivided into 2555 ( $6.46 \pm 0.13\%$ ) MSe1 stars, 2591 ( $6.56 \pm 0.13\%$ ) MSe2 stars, 463 ( $1.17 \pm 0.05\%$ ) MSe3 stars, and 520 ( $1.32 \pm 0.06\%$ ) MSe4 stars.

As we have done for the three canonical MS populations of  $\omega$  Cen (MSa, rMS and bMS), we show in Fig. 7 a Gaussian-smoothed version of the  $\Delta_{m_{F275W}-m_{F336W}}^N$  vs.  $\Delta_{m_{F336W}-m_{F438W}}^N$  chromosome maps for the MSd (left), the MSe (right) subpopulations. Isodensity contours are shown in green.

### 3.7. A brief discussion on the less-constrained subpopulations

In the previous subsections, we selected four subpopulations, namely: bMS2, MSd3, MSe3 and MSe4, for which the identification was less obvious than for the other subpopulations. In order to give the reader an additional point of view on this subject, we extracted histograms of the subpopulations of the bMS, MSd and MSe on the chromosome map as follow. Let us take the bMS as an example. We fitted a straight line to the barycenters of the three subpopulations (red line in panel a1 of Fig 8). Then, we rotated the chromosome map in such a way that the fitted line is parallel to the abscissa. The rotation point can be chosen arbitrarily, and we adopted the center point of the chromosome map, at location (0.5, 0.5). We computed the  $\pm 1 \sigma$  of the distribution of points along the vertical axis of the rotated plane (corresponding to the pink lines in panel a1), and constructed a histogram with all the stars within  $\pm 1 \sigma$  (in black in panel a2), and of each subpopulation again within  $\pm 1 \sigma$ . The histogram of each subpopulation is color-coded accordingly in panel (a2): bMS1 in blue, bMS2



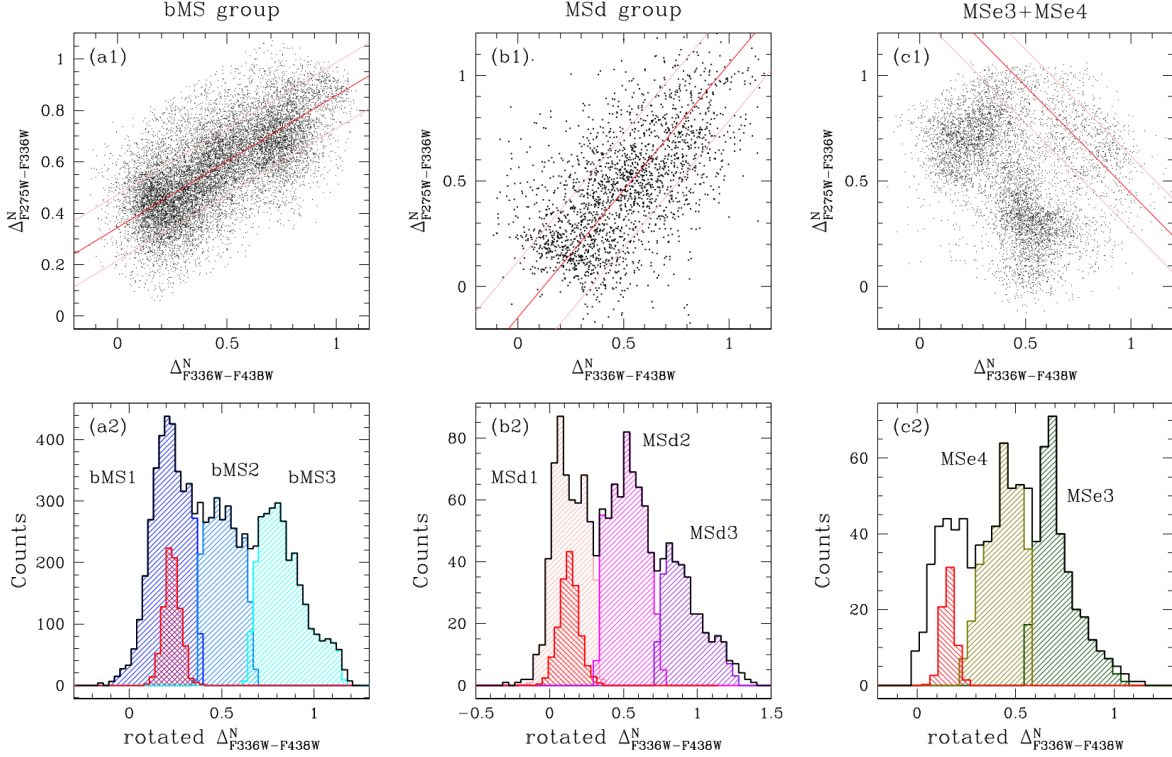


**Figure 8.** Top panels: replicas of the chromosome map for the bMS (left), the MSd (middle), and the MSe (right). In each panel, we fitted a straight line (in red) to the barycenters of the subpopulations within (only to the MSe3 and the MSe4 for the MSe), and rotated the plane in such a way that the fitted line becomes parallel to the abscissa. The rotation point is arbitrary: we chose the center point at (0.5, 0.5) in the chromosome map. We constructed a histogram (in black, bottom panels) using all stars within  $\pm 1\sigma$  along the ordinate distribution (pink lines). The histogram of each subpopulation, extracted within the pink lines, is color-coded. The histogram of photometric plus differential-reddening-correction errors only is shown in red. See the text for details.

in azure, and bMS3 in cyan. In addition, we derived the histogram of a distribution due to photometric and differential-reddening-correction errors alone (in red in a2). The height of the error histogram has been rescaled to be about half the height of the black histogram. This is not an issue because what is important is the width of the error histogram and not its height.

The histograms for MSd and MSe3+MSe4 stars were derived in the same way as for bMS stars, and are shown in panels (b2) and (c2), respectively. Note that the first peak in the histogram distribution of MSe3+MSe4 stars is due to the upper tail of the MSe2.

We can clearly see that the bMS3, the MSd3, and the MSe3 histogram distributions have an extended tail to the right side of the distribution, which might either indicate the presence of additional subpopulations, some sort of systematic selection effects, or might tell us that these subpopulations have experienced a prolonged period of star formation, over which chemical abundances have changed gradually.

We cannot exclude a-priori that what we have identified as the bMS2 (MSd3) is also due to an abundance spread within the bMS1 (MSd2) caused by a prolonged star formation, rather than distinct peaks associated with distinct subpopulation of the bMS (MSd). For the sake of argument, in what follows we will keep considering the bMS2 and the MSd3 as distinct subpopulations.

### 3.8. A qualitative estimate of the binary-fraction

There are still 4087 unidentified MS stars (or  $10.34 \pm 0.17\%$ ) in the magnitude interval  $20.16 \leq m_{F438W} \leq 22.36$ . First of all, we wanted to identify and remove as many binaries as possible, so that binaries will not bias any further attempt of identifying and tagging additional subpopulations. To this aim, we took advantage of the fact that, with the exclusion of MSa stars, all other  $\omega$  Cen subpopulations are almost overlapped to each other in the  $m_{F336W} - m_{F814W}$  CMD, which is illustrated in panel (a) of Fig. 9. The fiducial line of the 15 subpopulations identified so far are also shown, color-coded accordingly. Panel (b) is similar to panel (a), with the difference being that we removed the fiducial lines and all stars belonging to the MSa1 and the MSa2. Of the remaining 13 subpopulations, MSe3 and MSe4 stars are the reddest ones and (slightly) isolated from the others. For clarity, in panel (c) we show the same CMD as in panel (b) with just MSe3 and MSe4 stars highlighted with their corresponding colors.

To better isolate likely binary stars, we also removed MSe3 and MSe4 stars and plotted the remaining stars in panel (d). It is clear from the figure that the vast majority of the remaining 11 subpopulations lie on the blue side of the left-most green line (drawn by hand). The right-most green line, instead, defines the locus of MSa2+MSa2 equal-mass binaries. Since MSa2 stars are the reddest ones in this CMD, we expect no binaries redward of the right-most green line (besides, there

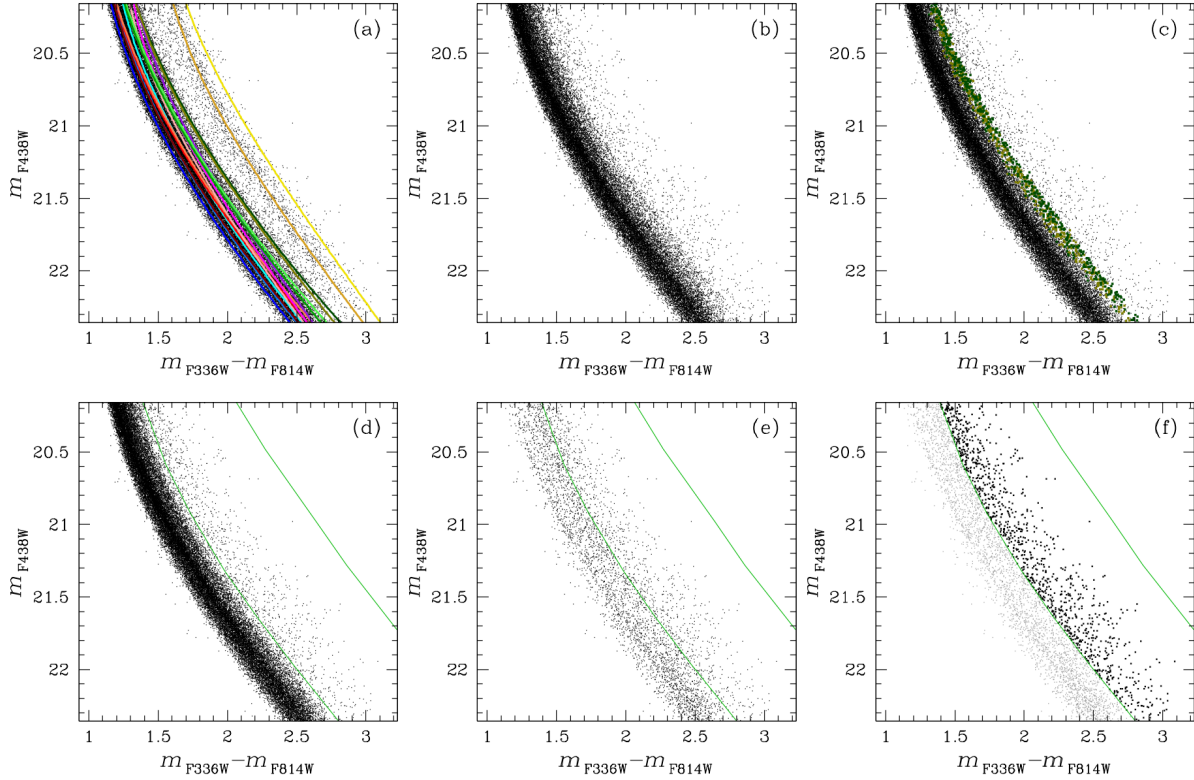


**Figure 9.** (a) the  $m_{F336W} - m_{F814W}$  CMD of  $\omega$  Cen between  $20.35 \leq m_{F438W} \leq 22.55$ . (b) same as (a), but we removed MSa1 and MSa2 stars. (c) same as (b), but we color-coded the redmost MSe3 and MSe4 subpopulations. (d) same as (c), but we also removed MSe3 and MSe4 stars. All other identified populations lie on the blue side of the left green line. The right green line shows the locus of MSa2-MSa2 equal-mass binaries, and no binary star can be redder than the right green line. (e) same as (b) but for unidentified stars only. We considered as binary stars all the unidentified stars between the two green lines. Binary stars are shown in black in panel (f), while the remaining unidentified stars are in gray.

are no stars redder than this line in the CMD).

Panel (e) of Fig. 9 shows the same CMD region of the previous panels, but this time we removed all stars belonging to the 15 previously-identified subpopulations. The two green lines in this panel are the same as in panel (d). Unidentified stars between the two green lines are potential binaries (shown in black in panel f), while stars bluer than the left-most green line (in gray in panel f) are expected to be a combination of: (i) binaries, (ii) stars belonging to already-identified subpopulations that have been somehow rejected during our selection procedures, and –possibly but less likely– (iii) a few badly-measured sources that somehow made it into our high-photometric-quality star list.

There are 1069 potential binaries ( $2.70 \pm 0.08\%$ ) in the magnitude interval  $20.16 \leq m_{F438W} \leq 22.36$  within the two green lines (in black in panel f). This estimate could in principle represent a lower limit, since more binaries can be present among the gray stars in panel (f). On the other hand, among the 1069 potential binaries we had identified could hide single stars with extreme chemical compositions (more in the next Section). Our binary estimate is by no mean intended to be rigorous, but it simply represents a convenient tool that will allow us to further dissect the MS of the cluster.

### 3.9. Are there more?

At this point, our TRSR iteration process is completed. No single CMD (or pseudo-CMD) can further help us in unraveling additional subpopulations. We can now have a look at where the 15 subpopulations lie on chromosome maps derived using the entire MS.

The top and middle panels of Fig. 10 show the  $\Delta_{m_{F275W} - m_{F336W}}^N$  vs.  $\Delta_{m_{F336W} - m_{F438W}}^N$  (top) and the  $\Delta_{C_{F275W, F336W, F438W}}^N$  vs.  $\Delta_{m_{F275W} - m_{F814W}}^N$  (middle) chromosome maps of the entire MS of the cluster within the magnitude range  $20.16 \leq m_{F438W} \leq 22.36$ . The chromosome-map plane of the top panels is the same we used in the previous subsections. Note that, this time, the fiducial lines used to rectify and parallelize the  $m_{F275W} - m_{F336W}$  and  $m_{F336W} - m_{F438W}$  CMDs had to necessarily enclose the entire color extension of the MS and not just that of any single population. As a consequence, the exact position of each star on the top panels of Fig. 10 is different from that occupied by the same star in the chromosome map of any previous figure. What matters here is the *relative* position of stars of different subpopulations with respect to each other.

The chromosome map of the middle panels is instead similar to the one extensively used by Milone et al. (2017a) to analyze the multiple populations on the RGB of 57 GCs (including that of  $\omega$  Cen). Milone et al. (2017a) used different fiducial lines to rectify both the  $m_{F275W} - m_{F814W}$  CMD and the  $C_{F275W, F336W, F438W}$  color index. Moreover, the convention was

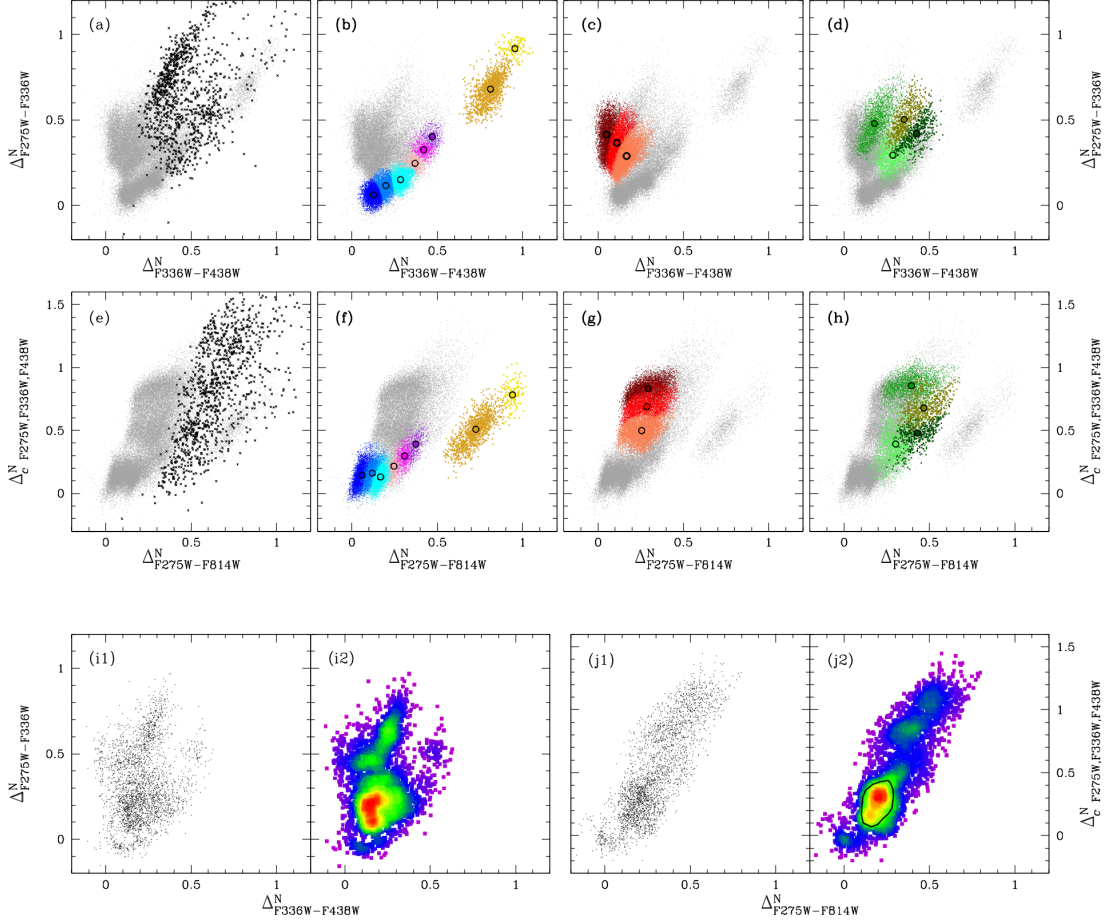


**Figure 10.** The top panels show the  $\Delta N_{m_{F275W}-m_{F336W}}$  vs.  $\Delta N_{m_{F336W}-m_{F438W}}$  chromosome map of the entire MS of  $\omega$  Cen within  $20.16 \leq m_{F438W} \leq 22.36$ . (a) MS single stars are in gray, while candidate binary stars are marked in black. (b) binary stars are removed, and MSa, bMS and MSd stars are color-coded according to their subgroups. The barycenter of each subpopulation is also marked with a solid circle with the corresponding color (as defined in the previous figures). (c) rMS stars are highlighted. (d) MSe stars are highlighted. The middle panels propose again the content of the top panels, but using a different chromosome map:  $\Delta N_{F275W, F336W, F438W}$  vs.  $\Delta N_{m_{F275W}-m_{F814W}}$ . Panels (i1) and (i2) show the  $\Delta N_{m_{F275W}-m_{F336W}}$  vs.  $\Delta N_{m_{F336W}-m_{F438W}}$  chromosome map and its Hess diagram, respectively, for stars that do not belong neither to any of the previously-identified subpopulations nor to the binary sample. Panels (j1) and (j2) show the  $\Delta N_{F275W, F336W, F438W}$  vs.  $\Delta N_{m_{F275W}-m_{F814W}}$  and its Hess diagram for the same previously-unidentified stars. The black boundary in panel (j2) encloses the main clump of stars. See the text for details.

used here for the y axis of the middle panels in Fig. 10 is opposite to that adopted by Milone et al. (2017a), so a more direct comparison with the work of Milone et al. (2017a) would require an upside-down flip of our middle panels. Again, what matters here is the relative position occupied by stars of different subpopulations.

In each of the top and middle panels, gray points represent MS single stars. Selected binary stars are only shown in black in panels (a) and (e), for reference. Let us briefly return to our binary selections. If we compare the chromosome maps of Fig. 10 with that in Fig. 6 of Milone et al. (2017a) (but mind the flip of the vertical axis) obtained for RGB stars, we can see that most of the objects that are classified here as binaries would occupy the same region as single stars with extreme [Fe/H], s-element, and C, N, and O abundances of Milone et al. (2017a). The MS-based and the RGB-based chromosome maps are similar but not identical, and while it is possible that the different populations of  $\omega$  Cen would maintain the same relative positions in the two planes, this cannot be taken as a given. A deeper investigation, beyond the scope of the present paper, is needed to solve this issue. For now, we stress that out

binary selections are not rigorous, and they should be taken “cum grano salis”. For simplicity, we will keep referring to these stars simply as binaries.

In panels (b) and (f) of Fig. 10 we have highlighted bMS, MSd and MSa subpopulations using the appropriate color-coding. The barycenter of each subpopulation is also marked by a colored solid circle. It is interesting to note that bMS, MSd and MSa stars appear to be more or less aligned in panel (b), and are the bluest subpopulations in  $\Delta N_{F275W, F336W, F438W}$  at any given value of  $\Delta N_{m_{F275W}-m_{F814W}}$  (panel f). These common features suggest that bMS, MSd and MSa stars must share some similarities in their chemical composition.

The three rMS subpopulations are highlighted in panels (c) and (g), while panels (d) and (h) show MSe stars. It is interesting to note that rMS stars are aligned almost perpendicularly to the direction defined by bMS, MSd and MSa stars in panel (c). Moreover, the three rMS subpopulations are aligned almost vertically in panel (g). It is less obvious to find common features for MSe stars, other than the fact that they occupy a well-defined region in both chromosome maps. Nevertheless, if we were to tear the MSe apart and independently consider

the doublets (MSe1 + MSe2) and (MSe3 + MSe4), then it would become apparent that both doublets share similar properties with those of rMS stars. The two doublets are both aligned vertically in the chromosome map of the middle panels and are both aligned perpendicularly to the direction defined by bMS, MSd and MSa stars in the chromosome map of the top panels. It might make more sense to actually separate the MSe subpopulations into two distinct groups, with a new MSe formed by MSe1 and MSe2 stars, and –say– a new MSf formed by MSe3 and MSe4 stars. For now, however, such a separation does not seem sufficiently justified, and we will keep considering the MSe1, MSe2, MSe3 and MSe4 stars together within the same MSe group.

Finally, in the bottom panels of Fig. 10 we show the chromosome maps and the companion Hess diagram for the remaining, so-far unidentified 3018 stars. Panels (i1) and (i2) refer to the  $\Delta_{m_{F275W}-m_{F336W}}^N$  vs.  $\Delta_{m_{F336W}-m_{F438W}}^N$  plane, while panels (j1) and (j2) refer to the  $\Delta_{C_{F275W,F336W,F438W}}^N$  vs.  $\Delta_{m_{F275W}-m_{F814W}}^N$  plane.

The bottom panels reveal the presence of a prominent, well-defined clump of stars, together with a few other lesser overdensities. The main clump, located at about (0.15,0.15) in panel (i2) and at about (0.2,0.3) in panel (j2), is formed by the same stars in both chromosome maps and peaks about half-way between the barycenters of bMS and rMS stars. Some of the other lesser overdensities in the bottom panels might also be genuine new subpopulations of  $\omega$  Cen, but there is a non-negligible chance that they might also be the end-result of the conservative selection cuts we applied during the population-tagging processes described in the previous subsections. Moreover, some of these smaller clumps share the same location of other subpopulations in one or both chromosome maps, or they are suspiciously close to the regions occupied by binary stars to make us think they might be binary stars as well.

The main clump is rounder and more compact in panel (j2), and possibly exhibits a tail of points extending towards smaller  $\Delta_{C_{F275W,F336W,F438W}}^N$  values. Let us temporarily identify the stars in this clump as MSx stars. At first, we thought the MSx might constitute a new, genuine subpopulation of  $\omega$  Cen. We selected all MSx stars within a the black boundary shown in panel (j2), and plotted them in all the available CMDs. If the MSx were to be a genuine subpopulation, then MSx stars would define a single sequence in CMDs. It turned out that MSx stars appear to be split into two, sometimes three segmented sequences in different CMDs. It was clear that the MSx is none other than a collection of stars belonging to other subpopulations that were rejected preferentially in different magnitude intervals. We will not discuss the specious MSx any further. Since the main clump of unidentified stars in the chromosome maps do not constitute an additional population of  $\omega$  Cen, the chances for the lesser clumps to be themselves additional populations are possibly even smaller than those for the MSx.

#### 4. MULTIPLE-POPULATION OVERVIEW

In the previous Section we described in detail how we were able to photometrically isolate distinct MS populations (and their subpopulations) in  $\omega$  Cen. The main observational findings can be summarized as follows:

- We confirmed the findings of Bellini et al. (2010) of a split MSa;

- We found that both the bMS and the rMS are each formed each by three subpopulations of stars (the rMS was previously shown to be split into two branches, see Bellini et al. 2010);
- We discovered a new population, the MSd, made up by three subpopulations, sharing similar properties to bMS and MSa stars;
- We discovered another new population, the MSe, comprised of four subpopulations, sharing similar properties to rMS stars;

Figures 11, 12 and 13 show all the possible CMDs that can be obtained by combining the five filters at our disposal (keeping  $m_{F438W}$  as the ordinate), zoomed-in around the MS and SGB regions. For completeness, in Fig. 13 we also included the  $C_{F275W,F336W,F438W}$  (bottom left) and the  $C_{F336W,F438W,F814W}$  (bottom right) pseudo-CMDs. The  $C_{F336W,F438W,F814W}$  pseudo-CMD represents the *HST* equivalent of the  $C_{UBI}$  index (see, e.g., Monelli et al. 2013). We included in each panel of these figures the fiducial line of the 15 subpopulations, color-coded accordingly. For a better reading of the figures, identified stars are now shown in gray.

We have based our population-tagging procedures on CMDs and chromosome maps. Because of that, it was impossible to separate the different subpopulations (besides the MSa group) for magnitudes brighter than  $m_{F438W} \sim 20$ . If we had also made use of pseudo-CMDs (see, e.g., the bottom panels of Fig. 13), we might have been able to push our selections one magnitude brighter. Including pseudo-CMDs in our selection procedures would have added an extra layer of complexity that goes beyond the scope of the present paper. The connection between the cluster's multiple populations at different evolutionary stages will be the subject of a forthcoming paper. We will use pseudo-CMDs to help us push the SGB selections to one magnitude below the turn-off. This way, we will be able to directly follow the 15 subpopulations from the MS up to the base of the RGB.

Some interesting subpopulation properties can be observed in these CMDs:

- The MSa1 and MSa2 stars never cross each other. These two subpopulations are typically well separated from the others when the CMD color is based on the F275W or the F336W filters. On the other hand, MSa1 and MSa2 stars *do overlap* with the rMS and the MSe in the  $m_{F606W}-m_{F814W}$  CMD.
- Of the three bMS subpopulations, the bMS1 is always the bluest one and the bMS3 always the reddest one when the CMD color is based on the F275W or the F336W filters, but the bMS3 becomes the bluest one in the  $m_{F606W}-m_{F814W}$  CMD. The bMS as a whole is typically the bluest population in all CMDs, with two notable exceptions: the rMS is the bluest one in the  $m_{F336W}-m_{F438W}$  CMD, and the MSd is the bluest one in the  $m_{F606W}-m_{F814W}$  CMD.
- The rMS1 is the reddest of the three rMSs when the CMD color is of the form  $m_{F336W}-X$ , with X being any other redder filter, but the opposite happens in the  $m_{F275W}-m_{F336W}$  CMD. Moreover, when the CMD color is of the form  $m_{F275W}-X$ , the three rMSs appear to curve towards redder colors at the faint end more than



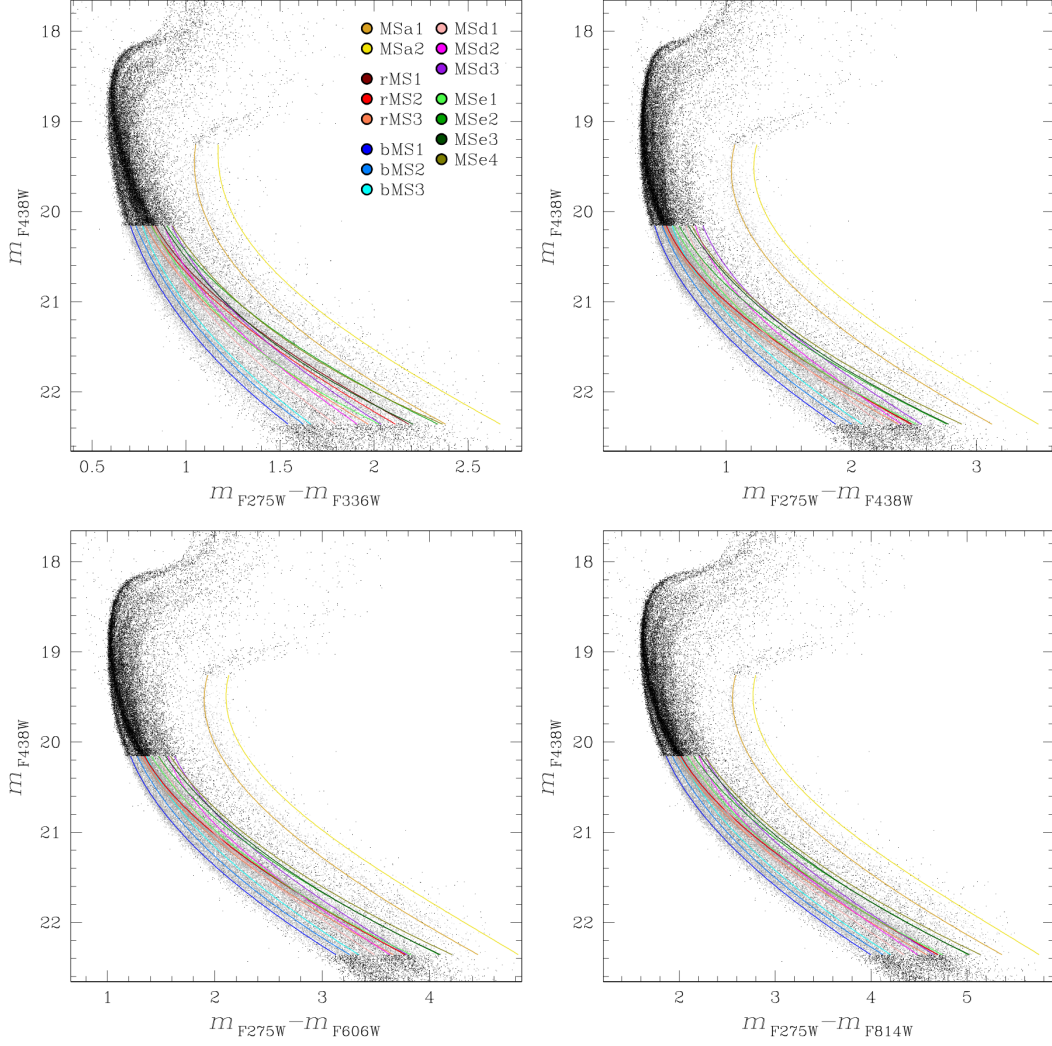


**Figure 11.** The  $m_{F275W} - m_{F336W}$ ,  $m_{F275W} - m_{F438W}$ ,  $m_{F275W} - m_{F606W}$  and  $m_{F275W} - m_{F814W}$  CMDs centered on the MS and SGB of  $\omega$  Cen. Identified stars are now in gray. Fiducial lines for each of the 15 subpopulations are color-coded accordingly.

any other subpopulation (with the possible exception of the MSe3 and the MSe4).

- The three MSd subpopulations (in particular the MSd2 and the MSd3) become increasingly more isolated the closer to the bright limit in the  $m_{F336W} - m_{F438W}$  CMD, where they can easily be followed beyond the bright magnitude limit that we applied, all the way to the base of the RGB. It seems clear that the SGB-D group discussed in Villanova et al. (2014) (called SGB4/MrI group by Tailo et al. 2016) is the progeny of the MSd.
- The three MSd subpopulations are as blue as the bMS in the  $m_{F438W} - X$  CMDs, but are the among the reddest populations (excluding MSa stars) in the  $m_{F336W} - m_{F438W}$  CMD, and are generally overlapped with rMS and MSe stars in  $m_{F275W} - X$  CMDs.
- Stars of the MSe2 and the MSe4 are always redder than the three rMS subpopulations (but just marginally so in the  $m_{F606W} - m_{F814W}$  CMD).
- MSe1 and MSe3 stars are generally bluer than MSe2

and MSe4 stars, but typically redder than rMS stars in most CMDs.

- In the  $C_{F336W,F438W,F814W}$  pseudo-CMD, the MSe2 is generally overlapped with rMS stars, while MSe1, MSe3 and MSe4 stars overlap with bMS stars.
- In the  $C_{F275W,F336W,F438W}$  pseudo-CMD, MSe2 stars are the reddest on average.

## 5. QUALITATIVE ABUNDANCE ANALYSIS

In hopes of shedding more light onto this complicated observational picture, we followed the powerful approach of looking at the color separation of the 15 MS subpopulations as a function of the color index in which they are observed (see, e.g., Bellini et al. 2010, 2013b; Milone et al. 2012b, 2013, 2015b). This analysis is also aimed at providing some qualitative information for future interpretations of our findings,

To do this, we measured the color difference ( $\Delta\text{color}$ ) between the rMS1, chosen as a reference, and each subpopulation. The color difference is measured in all CMDs of

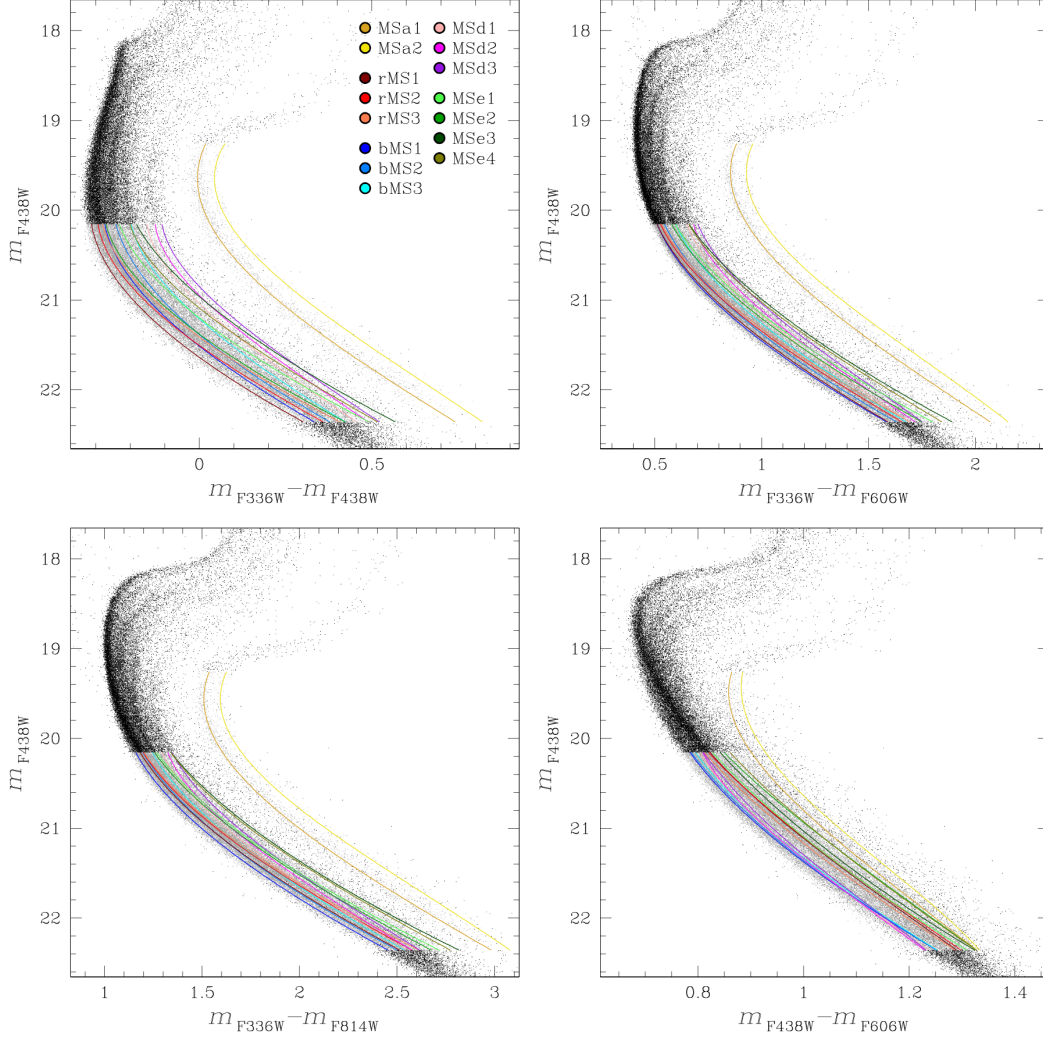


**Figure 12.** Similar to Fig. 11 but for the  $m_{F336W} - m_{F438W}$ ,  $m_{F336W} - m_{F606W}$ ,  $m_{F336W} - m_{F814W}$  and  $m_{F438W} - m_{F606W}$  CMDs.

the form  $X - m_{F438W}$  or  $m_{F438W} - X$  (depending on the filter  $X$  being bluer or redder than F438W, respectively) at the fixed magnitude level of  $m_{F438W} = 21.5$ . In this section, we extended the analysis to all the UVIS filters at our disposal except for the the F350LP, F850LP (the two long-pass filters) and the medium-band F390M (similar to the F390W but with poorer photometry). Note that we are keeping both F656N and F658N filters. The former selects the  $H_\alpha$  line, while the latter selects the continuum after the  $H_\alpha$  line. Finally, we are not considering the case  $X = m_{F438W}$ , since all the corresponding  $\Delta\text{color}$  values are identical to zero (by construction).

Figure 14 shows, for each subpopulation, the  $\Delta\text{color}$  values as a function of the central wavelength (in nm) of the  $X$  filter. Each row of panels in the figure refers to a different population, from the MSa on the top to the MSe on the bottom, and are organized in the same order we have selected them in Sect. 3. The panels within each row refer to the different subpopulations of a given population group. The scale in the abscissa is kept fixed in all panels, but the scale in the ordinate is only kept fixed within a given population group, so that we can appreciate both the small  $\Delta\text{color}$  differences between the rMS subpopulations and the larger differences between the MSa subpopulations and the reference rMS1. A

gray horizontal line at  $\Delta\text{color} = 0$  in each panel indicates no color differences with respect to the rMS1 and is meant to better guide the eye. We included a colored arrow at the end of the top row to better read the direction of the  $\Delta\text{color}$ .

We collected the  $\Delta\text{color}$  profiles of Fig. 14 into two groups sharing similar properties. The first group contains those subpopulations having increasing  $\Delta\text{color}$  values for  $\lambda \geq 336$  nm, while the second group is made up by those subpopulations with constant  $\Delta\text{color}$  values for  $\lambda \geq 438$  nm. The bMS is the archetype of the former group, and the rMS is the archetype of the latter group. The  $\Delta\text{color}$  profiles of these two groups are shown in Fig. 15. There is an interesting gradual  $\Delta\text{color}$ -value decrease moving from the bMS1 to the MSa2 (left panel). On the other hand, the subpopulations on the right panel seem to split into 2 subgroups for  $\lambda < 300$  nm: the subgroup (MSe2–4) has increasingly negative  $\Delta\text{color}$  values at shorter wavelengths, while the subgroup (rMS1–3+MSe1) reaches a minimum negative  $\Delta\text{color}$  at  $\lambda = 336$  nm before returning to  $\Delta\text{color}$  values close to zero at shorter wavelength.

There are several stellar-abundance-variation effects dictating the behavior of each profile we see in Figs. 14 and 15:

*C, N, O:* The F275W, F336W and F438W bandpasses include the OH, HN, and CN+CH molecular bands, respec-



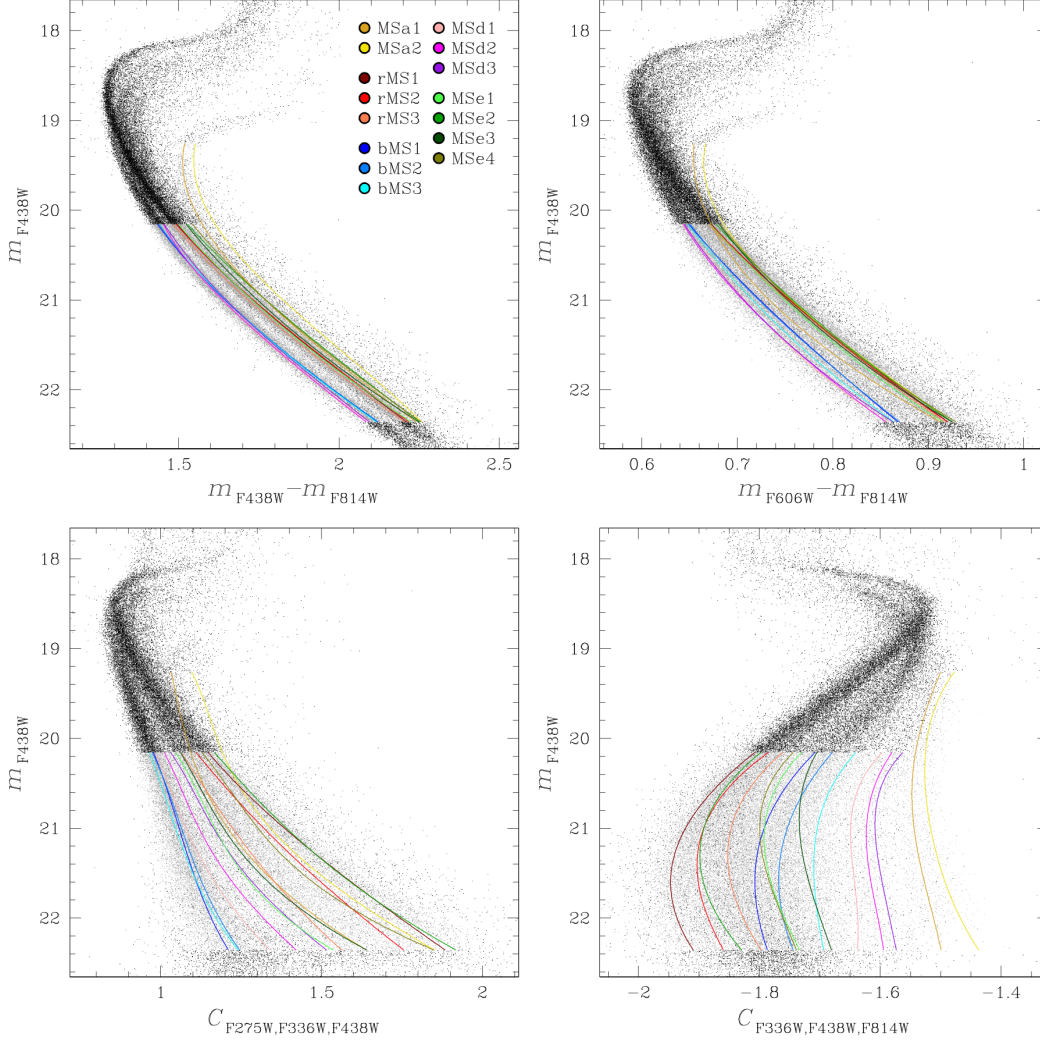


**Figure 13.** Similar to Fig. 11 but for the  $m_{F438W} - m_{F814W}$  and  $m_{F606W} - m_{F814W}$  CMDs and the two pseudo-CMDs  $C_{F275W, F336W, F438W}$  and  $C_{F336W, F438W, F814W}$ .

tively. First-generation (1G) stars are N-poor but O- and C-rich. As a result, all other things being equal, 1G stars tend to be brighter in F336W and fainter in F275W and F438W with respect to second-generation (2G) stars, which are N-rich but C- and O-poor (see, e.g., Milone et al. 2013 for a detailed description and modeling of this phenomenon). As a consequence, the higher the N abundance (and consequently the lower C and O abundances), the deeper the negative  $\Delta\text{color}$  peak at  $\lambda=336$  nm, and the higher the rise at  $\lambda=225\text{--}275$  nm.

**Helium:** Optical filters are less sensitive to C, N, and O variations, but offer a good proxy to temperature (and therefore helium) variations. He-rich, 2G stars tend to have increasingly higher  $\Delta\text{color}$  values at longer optical wavelengths the higher their He content (Milone et al. 2013).

**Iron:** The effects of different Fe abundances on the  $\Delta\text{color}$  profiles are harder to quantify. To zeroth order, Fe and He have similar effects on the stellar surface temperature. In principle, the Fe-abundance could be estimated using the bluer part of the profiles. In practice, the bluer part of the profiles is dominated by light-element variations. Detailed Fe and C, N, and O abundances have been published in the past for  $\omega$  Cen RGB stars (e.g., Johnson & Pilachowski 2010; Marino et al.

2011, 2012) and SGB stars (e.g., Villanova et al. 2014). A possible solution could be to link each of the 15 MS subpopulations identified in this work with their counterparts on the SGB and RGB, but this goes far beyond the purpose of this paper, which is the detailed photometric analysis of the multiple populations of  $\omega$  Cen along the MS. We plan to address this topic in a forthcoming paper in this series.

In order to better understand the subpopulation trends we see in Figs. 14 and 15, we compared the observed  $\Delta\text{color}$  values with those predicted by appropriate synthetic spectra (e.g., Milone et al. 2012b, 2013, 2014; Bellini et al. 2013b). The spectra are computed for MS stars at a fixed magnitude of  $m_{F438W}=21.5$ .

We assumed for the reference subpopulation rMS1 the following values:  $[\alpha/\text{Fe}]=0.3$ ,  $Y=0.25$  (typical of a 1G population),  $[\text{Fe}/\text{H}]=-1.7$ ,  $[\text{C}/\text{Fe}]=0.4$ ,  $[\text{N}/\text{Fe}]=0.2$ ,  $[\text{O}/\text{Fe}]=0.3$  (the latter three being typical values for rMS stars, see, e.g., Johnson & Pilachowski 2010; Marino et al. 2011, 2012; Milone et al. 2017b). Effective temperature and gravity values are based on the best-fitting Dartmouth isochrones (Dotter et al. 2008), obtained by assuming a distance modulus  $(m-M)_0=13.69$  and a reddening  $E(B-V)=0.13$ , similar to the values quoted in

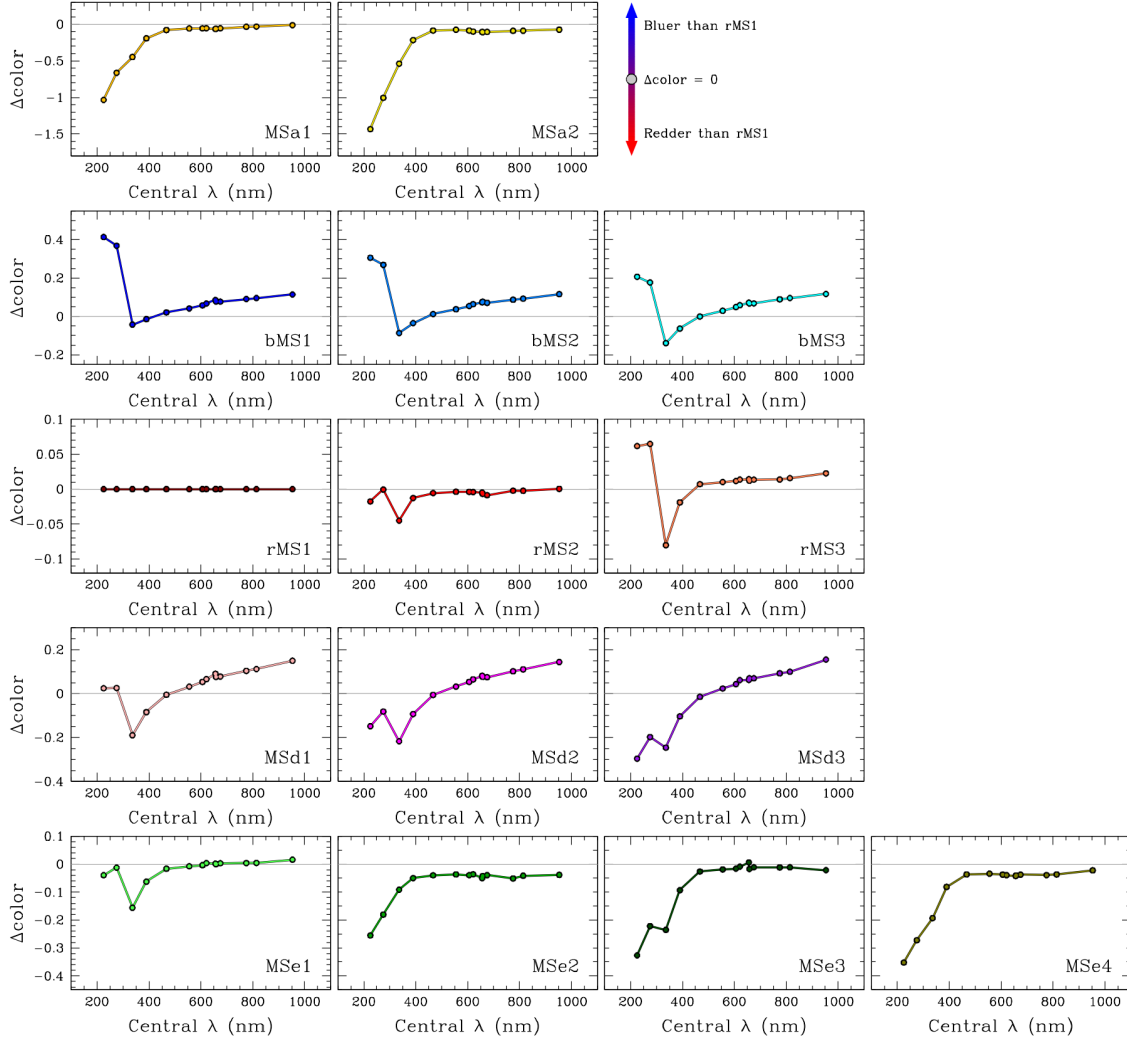


**Figure 14.** Color difference ( $\Delta\text{color}$ ) between each subpopulation and the rMS1 (chosen as a reference) as measured in different CMDs of the form  $X - m_{\text{F438W}}$  or  $m_{\text{F438W}} - X$ , where  $X$  is any of filter other than F438W. The  $x$  axis shows the central wavelength of the  $X$  filter. The  $\Delta\text{color}$  values are measured at the fixed magnitude level of  $m_{\text{F438W}}=21.5$ . Positive/negative  $\Delta\text{color}$  values imply that a given subpopulations is bluer/redder than the rMS1. Note that, in each panel, the vertical scale is kept fixed within each population group, but it varies for different groups. By definition, all  $\Delta\text{color}$  values of the reference subpopulation rMS1 are equal to zero, and are shown here only for completeness.

Harris (1996), and an age of 13.5 Gyr. The adopted chemical and physical values were then used as input parameters for the ATLAS12 and SYNTHE codes (Castelli 2005; Kurucz 2005; Sbordone et al. 2007) to generate a grid of synthetic spectra in the wavelength range between 220 and 960 nm. These spectra were then integrated over the transmission curves of the WFC3/UVIS filters used in this work.

Next, we synthesized stellar spectra for six populations characterized by different  $[\text{Fe}/\text{H}]$ ,  $Y$ , and  $C, N, O$  abundances. The results of these simulations are summarized in Fig. 16. Panel (a) shows how the  $\Delta\text{color}$  varies as a function of wavelength if we only assume different  $[\text{Fe}/\text{H}]$  abundances with respect to the reference subpopulation. We adopted iron abundances typical of the bMS ( $[\text{Fe}/\text{H}]=-1.4$ ) and of the MSA ( $[\text{Fe}/\text{H}]=-0.7$ ). In panel (b) we kept the same iron abundance of the reference population, and we assumed two different helium abundances that are typical of the extreme 2G populations in  $\omega$  Cen (Bedin et al. 2004; Norris 2004; Piotto et al. 2005). Panel (c) illustrates the behavior of a population simi-

lar to the rMS1 in terms of iron and helium, but with different  $C, N$ , and  $O$  abundances. Finally, in panel (d) we show the effects of different  $C, N$ , and  $O$  abundances on a population with primordial helium but  $[\text{Fe}/\text{H}]$  typical of the bMS.

By comparing the simulation results in Fig 16 to the  $\Delta\text{color}$  trends of the 15 populations in Figs. 14 and 15, we can qualitatively conclude the following:

- The subgroups of the bMS and the MSd are consistent with stellar populations highly enriched in both He and Fe with respect to the rMS1. Indeed, only a high He abundance can explain the increasing trends at longer optical wavelengths (panel b of Fig. 16), making a sequence—all other things being equal—bluer in optical CMDs. (Variations in Fe and/or  $C, N$ , and  $O$  alone can only produce a flat trend at optical wavelengths, see panels a and c.) High Fe abundances must also be present to counter-balance/mitigate what would otherwise be a very steep increase of the trend at shorter wavelengths, also due to He. Since bMS stars are

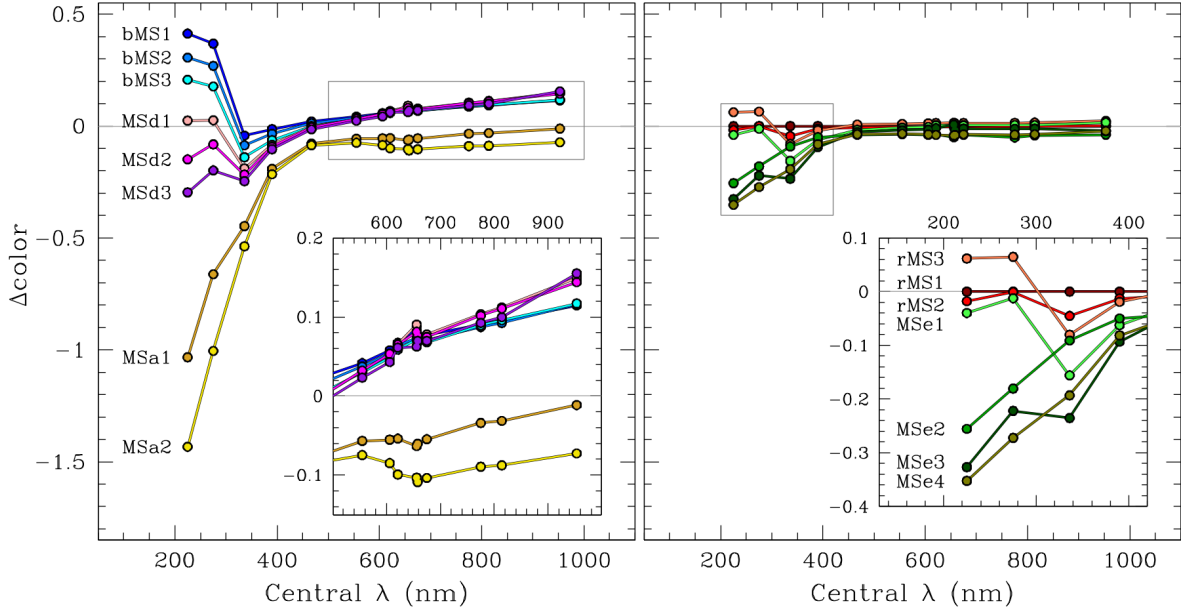


**Figure 15.** The  $\Delta\text{color}$  values of each subpopulations of Fig. 14 are collected in two groups: on the left those subpopulations sharing similar properties to the bMS, and on the right those subpopulations sharing similar properties to the rMS. On the left, all subpopulations show generally increasing  $\Delta\text{color}$  values for  $\lambda \geq 336$  nm. Below  $\lambda = 336$  nm, there is a gradually decreasing trend of the subpopulations, with the bMS1 reaching the highest  $\Delta\text{color}$  value at  $\lambda = 225$  nm, while the MSa2 reaches the lowest  $\Delta\text{color}$  value at the same  $\lambda$ . On the right, all subpopulations show a rather constant  $\Delta\text{color}$  value for  $\lambda \geq 438$  nm, but then split into 2 groups (rMS1–3 + MSe1) and (MSe2–4) moving to shorter  $\lambda$ . The inset in each panel shows a zoomed-in view around some key characteristics of the each group.

known to have a  $[\text{Fe}/\text{H}]$  of about  $-1.4$ , an even higher  $[\text{Fe}/\text{H}]$  value must be assumed for MSd stars, because of the less-positive trend at shorter wavelengths. The bMS and MSd groups also show evidence of N enrichment and C/O depletion, as inferred from the dip in the color profiles at 336 nm (i.e., using the F336W filter).

- The rMS2, the rMS3 and the MSe1 should have a similar (low) Fe content to the rMS1, but different C, N, and O abundances. The rMS2 and the MSe1 should also have a similar He content to that of the rMS1, while the rMS3 could slightly more Fe rich than the reference population (because of the decreasing trend at shorter wavelengths).
- The observed pattern of the remaining three MSe subpopulations (MSe2, MSe3, and MSe4) seems mostly due to (small) iron variations, with possibly the MSe3 showing the signature of N differences.
- The two MSa subpopulations are likely to be strongly enhanced in both iron and helium. As it is the case for bMS and MSd stars, only a high He abundance can explain the increasing trends at longer optical wavelengths. Moreover, a much higher Fe abundance than MSd stars must be assumed to completely reverse what would otherwise be an increasing, He-induced trend at shorter wavelengths. In fact, this is what we measure from spectra of RGB stars: the  $[\text{Fe}/\text{H}]$  abundance of the RGB equivalent of MSa stars (the so-called RGBa stars) is of about  $-0.8$  (Johnson & Pilachowski 2010; Marino et al. 2012).

TABLE 1  
MULTIPOPULATION COMPONENTS OF THE MS OF  $\omega$  CEN  
IN THE MAGNITUDE RANGE  $20.16 < m_{\text{F438W}} < 22.36$

MAIN GROUP	SUBGROUP	$N_{\text{Stars}}$	FRACTION	Fe	He	N
Entire MS		39 526	100%			
MSa		1394	$3.53 \pm 0.10\%$			
	MSa1	1283	$3.25 \pm 0.09\%$	+++	+++	?
	MSa2	111	$0.28 \pm 0.03\%$	+++	+++	?
bMS		12 776	$32.32 \pm 0.33\%$			
	bMS1	5141	$13.01 \pm 0.19\%$	+	+++	++
	bMS2	3683	$9.32 \pm 0.16\%$	+	+++	++
	bMS3	3952	$10.00 \pm 0.17\%$	+	+++	++
rMS		13 124	$33.20 \pm 0.33\%$			
	rMS1	3739	$9.46 \pm 0.16\%$	–	–	–
	rMS2	3838	$9.71 \pm 0.16\%$	–	–	+
	rMS3	5547	$14.03 \pm 0.20\%$	–	–	+
MSd		2016	$5.10 \pm 0.12\%$			
	MSd1	757	$1.92 \pm 0.07\%$	++	++	+
	MSd2	819	$2.07 \pm 0.07\%$	++	++	+
	MSd3	440	$1.11 \pm 0.05\%$	++	++	+
MSe		6129	$15.51 \pm 0.21\%$			
	MSe1	2555	$6.46 \pm 0.13\%$	–	–	+
	MSe2	2591	$6.56 \pm 0.13\%$	+	–	–
	MSe3	463	$1.17 \pm 0.05\%$	+	–	+
	MSe4	520	$1.32 \pm 0.06\%$	+	–	–
Binaries <sup>(†)</sup>		1069	$2.70 \pm 0.08\%$			
Unidentified		3018	$7.64 \pm 0.14\%$			

(†) Included here for completeness.

## 6. CONCLUSIONS

The exquisite photometric performance of *HST*, in particular in the near-UV regime, has allowed us to undertake for the first time an extensive multi-color analysis of the MS of the GC  $\omega$  Cen. The main results of this analysis can be

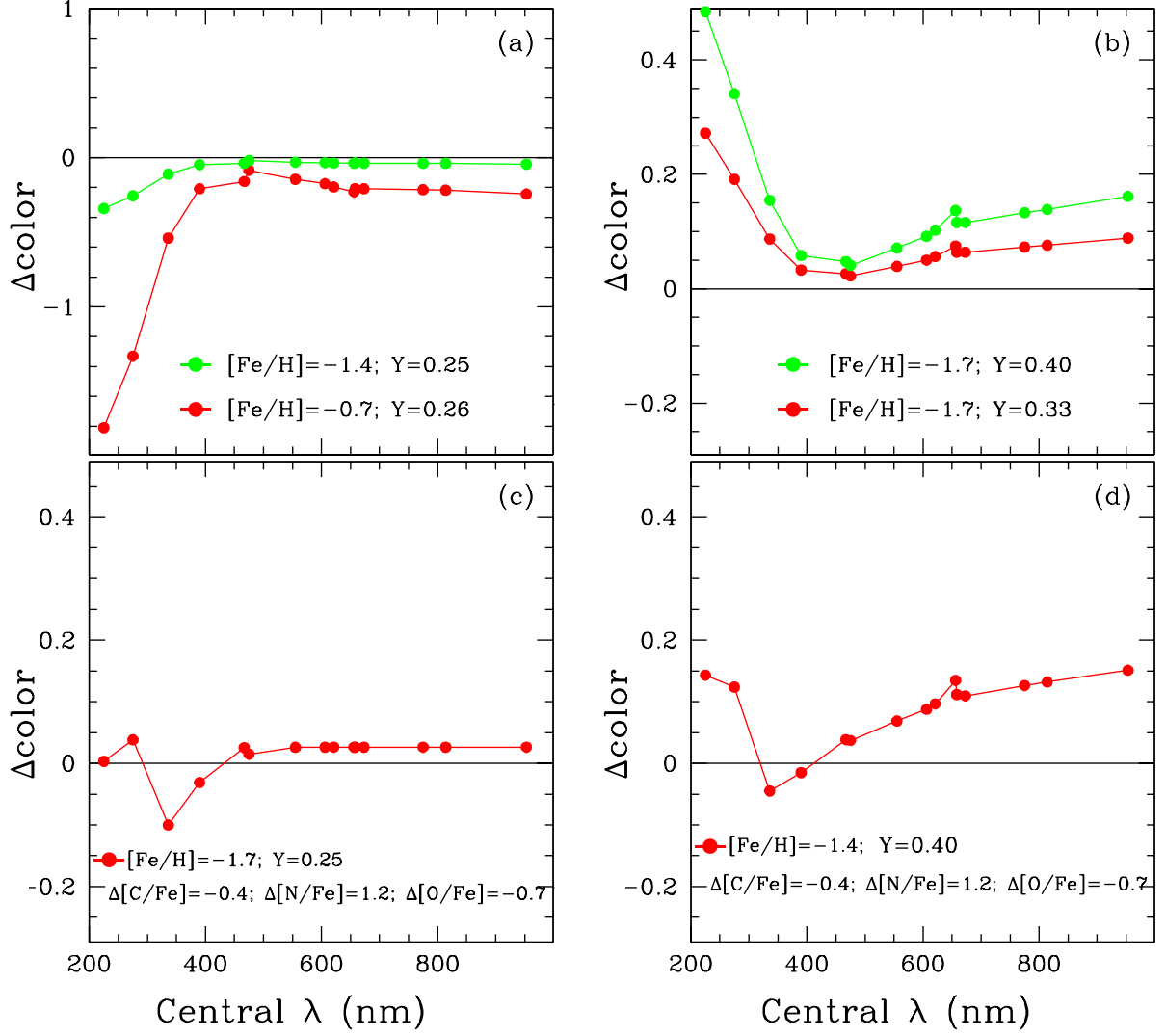


**Figure 16.** This figure shows the expected  $\Delta\text{color}$  versus wavelength behavior of stellar populations with different Fe, Y, and C, N, and O abundances with respect to a reference population with a chemical composition resembling that of the rMS1. Panel (a) shows two simulated populations with the same C, N, O and Y composition of the rMS1, but different  $[\text{Fe}/\text{H}]$  content ( $[\text{Fe}/\text{H}] = -1.4$  is typical of bMS stars, and  $[\text{Fe}/\text{H}] = -0.7$  is typical of MSa stars). In panel (b) we show the effects of different helium abundances with respect to the reference population, all other things being equal. The lower panels (c) and (d) illustrate the effects of changing Fe, He, C, N, and O, with results comparable to those of the two groups of populations with similar properties we collected in Fig. 15. See the text for details.

summarized as follows. We have confirmed the findings of Bellini et al. (2010) that the MSa is split into two subpopulations (named here MSa1 and MSa2). Recently, Milone et al. (2017b) identified six  $\omega$  Cen subpopulations along the faint MS of the cluster, using exquisite *HST* optical and IR photometry of an external field (about  $17'$  from the cluster's center) from GO-9444, GO-10101 (both PI: King), GO-14118 and GO-14662 (both PI: Bedin). In particular, the authors found two extreme subpopulations, which they named S1 and S2 (Milone et al. 2017b, their Fig. 2). Both S1 and S2 subpopulations are expected to be highly He-enhanced ( $Y \sim 0.4$ ), and have an iron abundance  $[\text{Fe}/\text{H}]$  of  $-1.1$  and  $-0.7$ , respectively. Given the high iron abundance of the latter, it is likely that the subpopulation S2 of Milone et al. (2017b) is associated with the MSa.

We discovered that both the bMS and the rMS are actually split into three subcomponents (the rMS was previously

known to be split into two subpopulations, Bellini et al. 2010). Moreover, we discovered two additional population groups: the MSd and the MSe. The former is itself split into three subcomponents, sharing properties more similar to those of the bMS and the MSa. The latter is split into four subcomponents, with properties more similar to the rMS. Some of these subpopulations also show hints of further subdivisions. While it is tempting to link the four main population groups rMS, MSe, MSd and bMS to populations A, B, C, and D of Milone et al. (2017b), respectively, it is worth noting that the bMS and the rMS have a strong radial gradient (see, e.g., Sollima et al. 2007; Bellini et al. 2009). A clear association between the multiple subpopulations we have found in the core and those found by Milone et al. (2017b) at  $17''$  from the center of the cluster would require either a chemical tagging or a radial-gradient analysis of the relative population ratios.

In Sect. 3, we listed the relative number of stars in each sub-

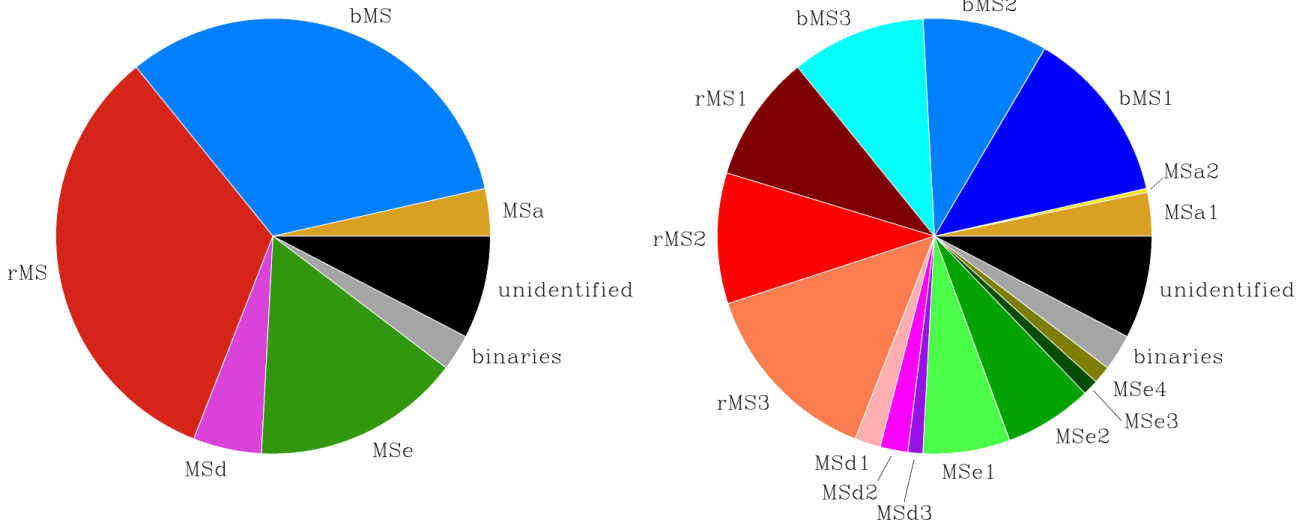


**Figure 17.** Pie charts of the MS composition of  $\omega$  Cen in the magnitude interval  $20.16 \leq m_{F438W} \leq 22.36$ . The five main population groups are shown on the left panel, while their partition into subpopulations is on the right panel.

population and their overall fraction with respect to the analyzed MS stars, but these numbers are reported in the text of the various subsections. For convenience, we have collected these pieces of information in Table 1. The quoted errors refer to Poisson errors only. Fractions are rounded off to the closest hundredth. It stands to reason that slightly different selections in the chromosome maps of each population would have led to (slightly) different subpopulation fractions. The main purpose of our selections is to allow us to infer qualitative properties of each subpopulation; they are not meant to be taken in an absolute sense. The quoted fractions for the five main population groups are more likely reliable to about 10%. The last three columns of Table 1 qualitatively show the iron, helium, and nitrogen relative abundances, respectively, with respect to the reference subpopulation rMS1, based on the comparison with synthetic spectra. One or more “+” signs indicate an increasingly high abundance, a “−” sign refers a relative abundance similar to that of the reference subpopulation, and a “?” means that that abundance cannot be qualitatively quantified with the tools at our disposal. The left panel of Fig. 17 shows a pie chart of the main population groups we found on the MS. In the right panel we further divided each population into its own subcomponents.

We have based our population-tagging procedures on CMDs and chromosome maps. Because of that, it would be hard to separate the different subpopulations (besides the MSa group) for magnitudes brighter than  $m_{F438W}=20.16$ . If we had also made use of pseudo-CMDs (see, e.g., the bottom panels of Fig. 13, we might have been able to push our selections one magnitude brighter. The connection between the cluster’s multiple populations on different evolutionary stages will be the subject of a forthcoming paper. We will use pseudo-CMDs to help us push the SGB selections to one magnitude below the turn-off. This way, we will be able to directly follow the 15 subpopulations from the MS up to the RGB.

We make publicly available with this paper a two-column

TABLE 2

MULTIPOPOPULATION IDENTIFIER	
Star ID	Population ID
1	0
2	0
3	0
4	0
5	0
...	...
17042	0
17043	5
17044	0
17045	7
17046	0
...	...

catalog with the adopted selections. The file contains 478 477 lines, one for each of the stars listed in the astro-photometric catalogs we published in Paper I. The first column contains the stellar ID numbers as defined in Paper I. Values in the second column allow the user to select stars belonging to the 15 subpopulations we have identified as follows: 1=MSa1, 2=MSa2, 3=bMS1, 4=bMS2, 5=bMS3, 6=rMS1, 7=rMS2, 8=rMS3, 9=MSd1, 10=MSd2, 11=MSd3, 12=MSe1, 13=MSe2, 14=MSe3, and 15=MSe4. A value of “0” refers to any other star in the astro-photometric catalog, including those that did not qualify for this analysis. An extract of the companion catalog is shown in Table 2.

**Acknowledgments.** AB acknowledges support from STScI grants AR-12656 and AR-12845. APM and AFM acknowledge support by the Australian Research Council through Discovery Early Career Researcher Awards DE150101816 and DE160100851. GP acknowledges partial support by PRIN-INAF 2014 and by the “Progetto di Ateneo 2014

## REFERENCES

- Anderson, J., Ph.D. thesis, Univ. of California, Berkeley, 1997
- Anderson, J. 2002, “Omega Centauri, A Unique Window into Astrophysics”, *Astronomical Society of the Pacific Conference Series*, 265, 87
- Bedin, L. R., Piotto, G., Anderson, J., et al. 2004, *ApJ*, 605, L125
- Bekki, K., & Freeman, K. C. 2003, *MNRAS*, 346, L11
- Bellini, A., Piotto, G., Bedin, L. R., et al. 2009, *A&A*, 507, 1393
- Bellini, A., Bedin, L. R., Piotto, G., et al. 2010, *AJ*, 140, 631
- Bellini, A., Anderson, J., Salaris, M., et al. 2013a, *ApJ*, 769, L32
- Bellini, A., Piotto, G., Milone, A. P., et al. 2013b, *ApJ*, 765, 32
- Bellini, A., Vesperini, E., Piotto, G., et al. 2015, *ApJ*, 810, L13
- Bellini, A., Anderson, J., Bedin, L. R., et al. 2017a, *ApJ*, 842, 6
- Bellini, A., Anderson, J., van der Marel, R. P., et al. 2017b, *ApJ*, 842, 7
- Cannon, R. D., & Stobie, R. S. 1973, *MNRAS*, 162, 207
- Castelli, F. 2005, *Memorie della Societa Astronomica Italiana Supplementi*, 8, 25
- Dotter, A., Chaboyer, B., Jevremović, D., et al. 2008, *ApJS*, 178, 89-101
- Johnson, C. I., & Pilachowski, C. A. 2010, *ApJ*, 722, 1373
- King, I. R., Bedin, L. R., Cassisi, S., et al. 2012, *AJ*, 144, 5
- Kurucz, R. L. 2005, *Memorie della Societa Astronomica Italiana Supplementi*, 8, 14
- Harris, W. E. 1996, *AJ*, 112, 1487, 2010 edition
- Hilker, M., & Richtler, T. 2000, *A&A*, 362, 895
- Lee, Y.-W., Joo, J.-M., Sohn, Y.-J., et al. 1999, *Nature*, 402, 55
- Marino, A. F., Milone, A. P., Piotto, G., et al. 2011, *ApJ*, 731, 64
- Marino, A. F., Milone, A. P., Piotto, G., et al. 2012, *ApJ*, 746, 14
- Milone, A. P., Piotto, G., Bedin, L. R., et al. 2012a, *A&A*, 540, A16
- Milone, A. P., Piotto, G., Bedin, L. R., et al. 2012b, *ApJ*, 744, 58
- Milone, A. P., Marino, A. F., Piotto, G., et al. 2013, *ApJ*, 767, 120
- Milone, A. P., Marino, A. F., Bedin, L. R., et al. 2014, *MNRAS*, 439, 1588
- Milone, A. P., Marino, A. F., Piotto, G., et al. 2015a, *MNRAS*, 447, 927
- Milone, A. P., Marino, A. F., Piotto, G., et al. 2015b, *ApJ*, 808, 51
- Milone, A. P., Piotto, G., Renzini, A., et al. 2017a, *MNRAS*, 464, 3636
- Milone, A. P., Marino, A. F., Bedin, L. R., et al. 2017b, *MNRAS*, 469, 800
- Monelli, M., Milone, A. P., Stetson, P. B., et al. 2013, *MNRAS*, 431, 2126
- Norris, J. E., & Da Costa, G. S. 1995, *ApJ*, 447, 680
- Norris, J. E. 2004, *ApJ*, 612, L25
- Pancino, E., Ferraro, F. R., Bellazzini, M., Piotto, G., & Zoccali, M. 2000, *ApJ*, 534, L83
- Piotto, G., Villanova, S., Bedin, L. R., et al. 2005, *ApJ*, 621, 777
- Piotto, G., Bedin, L. R., Anderson, J., et al. 2007, *ApJ*, 661, L53
- Piotto, G., Milone, A. P., Bedin, L. R., et al. 2015, *AJ*, 149, 91
- Sbordone, L., Bonifacio, P., & Castelli, F. 2007, *Convection in Astrophysics*, 239, 71
- Sollima, A., Ferraro, F. R., Bellazzini, M., et al. 2007, *ApJ*, 654, 915
- Tailo, M., Di Criscienzo, M., D’Antona, F., Caloi, V., & Ventura, P. 2016, *MNRAS*, 457, 4525
- van Leeuwen, F., Hughes, J. D., & Piotto, G. 2002, “Omega Centauri, A Unique Window into Astrophysics”, *Astronomical Society of the Pacific Conference Series*, 265
- Villanova, S., Geisler, D., Gratton, R. G., & Cassisi, S. 2014, *ApJ*, 791, 107